

Master Thesis



Escola Tècnica Superior  
d'Enginyeria Industrial de Barcelona

# An Electrochemical Impedance Spectroscopy Study of ZnI<sub>2</sub> Redox Flow Batteries

Author: **Benjamin Molinari**

Director: **Dra. Teresa Andreu**

Supervisor: **Dr. Sebastián Murcia-Lopez**



Barcelona, June 2019

# Acknowledgments

Over the last semester of thesis work, I have been fortunate to enjoy the support of a very knowledgeable group of professors and researchers. In addition, there are a few other individuals and things which have contributed to my success in other ways. I would like to thank some of them here.

First, to my thesis director Dra. Teresa Andreu for allowing me to carry out my thesis work here at IREC and for providing clarity and guidance when I was unsure of my work. To my advisor Dr. Murcia-Lopez for providing invaluable guidance in the lab and providing assurance after the many frustrating leakages I experienced. To my co-advisor Monalisa Chakraborty for the many explanations and discussions as well as lab and software help. Additionally, to Monalisa for providing the SEM images and charge-discharge analysis.

A salute to braccio di ferro champion Lorenzo Bigiani for his support with analysis software and fruitful discussions about the project. To the whole Energy Storage and Energy Harvesting group at IREC for being wonderful co-workers and dealing with my lack of spanish language skills; notably Carles, the impedance king, for his help with ZView analysis software.

A big hug of thanks to Christian Ribback for his inspiring work ethic and inspiring hummus. To fair-trade dark chocolate, trident gum, and fisherman's friends for the necessary post-lunch stimulation.

Last but not least, I would like to thank my brother, Dominic, and parents, Linda and Bill, for their scumtrulescent love and support.

# Chapter 1

## List of Acronyms Used

AC-	Alternating current	LCA-	Life cycle assessment
Ah-	Amp-hours	LCOE-	Levelized Cost of Energy
CE-	Charge Efficiency	mAh-	Milliamp-hours
CPE-	Constant phase element	ml-	Milliliter
CSP-	Concentrating solar power	MW-	Megawatt
DC-	Direct current	MWh-	Megawatt-hour
EE-	Energy Efficiency	NASA-	National Aeronautics and Space Administration
EIS-	Electrochemical Impedance Spectroscopy	NMR-	Nuclear Magnetic Resonance
ESS-	Energy Storage System	OCV-	Open circuit voltage
EV-	Electric vehicle	OHP-	Outer Helmholtz plane
GEIS-	Galvanostatic impedance spectroscopy	PEIS-	Potentiostatic impedance response
GW-	Gigawatt	PTFE-	Polytetrafluoroethylene
IHP-	Inner Helmholtz plane	PV-	Photovoltaic
IREC-	Institut de Recerca en Energia de Catalunya	RFB-	Redox flow battery
kg-	Kilogram	SEM-	Scanning Electron Microscopy
kW-	Kilowatt	TEM-	Transmission electron microscopy
kWh-	Kilowatt-hour	VE-	Voltage efficiency
		XRD-	X-ray diffraction

# Contents

<b>1</b>	<b>List of Acronyms Used</b>	<b>3</b>
<b>2</b>	<b>Abstract</b>	<b>7</b>
<b>3</b>	<b>Introduction</b>	<b>8</b>
3.1	Context . . . . .	8
<b>4</b>	<b>Background</b>	<b>12</b>
4.1	Methods of Grid Energy Storage . . . . .	12
4.2	Characteristics of Redox Flow Batteries . . . . .	20
4.3	Flow Battery State of Art . . . . .	23
4.4	Electrochemical Impedance Spectroscopy . . . . .	27
<b>5</b>	<b>Objectives and Scope</b>	<b>32</b>
<b>6</b>	<b>Experimental Methodology</b>	<b>34</b>
6.1	Electrochemical Cell Configuration . . . . .	34
<b>7</b>	<b>Results and Discussion</b>	<b>39</b>
7.1	Characterization of Full Cell . . . . .	39
7.2	Impedance Results . . . . .	44
7.3	Discussion and Further Improvements . . . . .	49
<b>8</b>	<b>Environmental Impact Analysis</b>	<b>51</b>
<b>9</b>	<b>Economic Analysis</b>	<b>52</b>
<b>10</b>	<b>Conclusion</b>	<b>54</b>

# List of Figures

3.1	Global levelized cost of energy (LCOE) of utility-scale renewable power generation, 2010-2018 [8] . . . . .	9
3.2	Global Energy storage capacity by Service/Use Case [7] . . . . .	10
3.3	Projected growth of United States domestic renewable energy generation [11] . . . . .	11
4.1	Energy storage technologies by discharge time and power ratings showing general use case parameter ranges [7] . . . . .	13
4.2	Electricity power system services offered by energy storage technologies [12] . . . . .	13
4.3	Diagram of a pumped hydro plant [14] . . . . .	14
4.4	Schematic of a compressed air storage plant [16] . . . . .	15
4.5	Diagram of thermal energy storage system supporting a wind power plant [19] . . . . .	16
4.6	Diagram of superconducting magnetic energy storage system [21] . . .	17
4.7	Basic diagram of a flywheel energy storage system [7] . . . . .	18
4.8	Schematic of a supercapacitor cell used for energy storage [14] . . .	19
4.9	Diagram of basic electrochemical cell [14] . . . . .	20
4.10	Diagram of basic all-vanadium redox flow battery [13] . . . . .	21
4.11	Installation of a redox-flow energy storage system supporting the generation of a solar power plant in Australia [22] . . . . .	22
4.12	Diagram of Zn-Br <sub>2</sub> redox flow battery [26] . . . . .	25
4.13	a) Graphical representation of the complexing of iodine (I <sub>2</sub> ) by bromide ions (Br <sup>-</sup> ). The structure of I <sub>2</sub> Br <sup>-</sup> and I <sub>3</sub> <sup>-</sup> ions are also shown in b) and c) [30] . . . . .	27
4.14	Characteristic Nyquist curve for an electrochemical battery cell displaying the general curve attributes [16] . . . . .	28
4.15	Nyquist plot of an all-vanadium battery showing distributed resistance in the high-frequency region [37] . . . . .	29

4.16 Diagram of Electrode/electrolyte interface showing the buildup of ions at the inner and outer Helmholtz planes (IHP and OHP respectively) which lead to a potential drop and the formation of a double layer capacitance $C_{dl}$ [35] . . . . .	31
6.1 Diagram of full cell components (not to scale) . . . . .	35
6.2 Full cell setup with peristaltic pump and electrolyte reservoir vials . . . . .	35
6.3 Vial of 1.5 M ZnI <sub>2</sub> + 1.5 M KI electrolyte solution . . . . .	36
6.4 Diagram of impedance cell components (not to scale). Note: Only one opening was used on each side while the other was blocked using Viton™ blocking piece on graphite current collector as seen below in fig.6.6. This way a single flow-through design was achieved. . . . .	37
6.5 Full cell with impedance cells setup with peristaltic pump and electrolyte reservoir vials . . . . .	37
6.6 Current collectors of impedance cells showing Viton™ gaskets used to help block flow channel and create flow through design . . . . .	38
7.1 SEM image of graphite foil used for anode of impedance cells [41] . . . . .	39
7.2 SEM images of thermally-treated carbon felt for cathode and anode of full cell as well as cathode of impedance cells [41] . . . . .	40
7.3 SEM image of metallic zinc deposit on carbon felt anode single fiber [41] . . . . .	40
7.4 SEM images of metallic zinc deposit on carbon felt anode bulk after cycling [41] . . . . .	41
7.5 Schematic of full cell setup used in this study [28] . . . . .	43
7.6 Charge/discharge analysis of full cell setup with Voltage, Coulombic, and Energy efficiencies [41] . . . . .	44
7.7 EIS Data of Single Cell with 2 charge cycles to 67% SoC . . . . .	45
7.8 EIS Data of cathode-side impedance cell at charge states 0, 15, 30, 45, and 60% SoC . . . . .	46
7.9 EIS Data of anode-side impedance cell at charge states 0, 15, 30, 45, and 60% SoC . . . . .	47
7.10 Equivalent circuit model of full cell . . . . .	48
7.11 Impedance response data of figure 10.2 with fit curves. . . . .	49
10.1 Single cell setup from first EIS runs [41] . . . . .	61
10.2 EIS run #2 of single cell setup . . . . .	61
10.3 Nafion membrane (a), and carbon felt (b) anode after cycling . . . . .	62

# Chapter 2

## Abstract

This thesis work focuses on the zinc-iodine redox flow battery system with an analysis of the electrochemical changes which occur throughout charge and discharge. A literature review of energy storage techniques was first carried out, focusing on flow batteries and the current state of art. The zinc-iodine system was chosen as the chemistry of focus due to its performance characteristics, promising newly published research on the subject, and its environmentally-safe chemistry. A  $\text{ZnI}_2$  redox flow cell was first designed and characterized with scanning electron microscopy (SEM) and charge-discharge analysis in order to verify its performance. The impedance response of the cell was then captured at various charge levels. Separate impedance cells were then used to effectively analyze the impedance responses of the anolyte and catholyte separately. The half cell responses after charge/discharge were determined to understand the electrochemical effects on each electrolyte as well as the system as a whole.

Upon cycling of the full cell, internal ohmic resistance, charge-transfer resistance, and double layer capacitance decreased significantly. The ohmic resistance change was attributed to the differences in solution resistance of the anolyte. During charge, an increase in  $\text{Zn}^{+2}$  ion mobility and migration of  $\text{K}^+$  ions, together led to lowering of solution resistance. Charge-transfer resistance was lowered due to the increase in available deposition sites and ease of this reduction reaction on the anode surface as  $\text{Zn}^{+2}$  was reduced to metallic zinc. The full cell was then cycled at various levels of charge while impedance cells were used to measure the impedance response of the half cells. The impedance responses of the catholyte and anolyte displayed different electrochemical effects. While the solution resistance of the catholyte increased with capacity due to the loss of free charge carriers, the charge-transfer resistance and double-layer capacitance decreased with state of charge (SoC) due to the deposition process of Zn. With a better understanding of the response of the individual half cells, electrolyte or cell material improvements could be recommended.

# Chapter 3

## Introduction

### 3.1 Context

#### Energy Storage and its Role in the Future Energy System

As the fact becomes increasingly clear that our earth has entered a new geological era defined by human impact, the public and private sector are continually pushed to make decisions to reduce their negative impacts on the natural world. Over the past 20 years, the concentration of CO<sub>2</sub> in the atmosphere has increased up to 10 times faster than any rise during the past 800,000 years [1]. Throughout this time, although they have very slow to make any effective change, it is clear that corporations and entire industries have been closely following climate models and using them to form strategy [2]. While governments throughout the world continue to promote strategies for limiting their emissions, the Intergovernmental Panel on Climate Change, suggests that more is needed. This leading global group of scientists and experts on the subject strongly urge that as a global community, we work to reach a warming limit of 1.5° above pre-industrial levels [3].

In order to attack this problem, it is logical to address the most significant impact areas first. Historically, the sector with the largest CO<sub>2</sub> contribution is electricity and heat generation. In 2006, this sector accounted for 42% of CO<sub>2</sub> generated globally [4]. With population growth and continued economic development, this global demand for energy is forecasted to increase by more than a quarter by 2040 [5]. With this growing demand for electrical energy coupled with both the urgency to de-carbonize the energy sector and the drastic drop in renewable energy prices compared to fossil fuels over the last decade (figure 3.1), these electricity sources are well-positioned to make up a significant role in the future energy system. However, with this shift in generation sources from fossil-fuel to renewables, the inherent intermittency of these natural sources becomes a challenge that needs to be addressed. Levels of solar and

wind generation often vary throughout the seasons but can also change on a minute-hourly timescale as passing clouds cover photovoltaic (PV) panels or the wind ceases for short periods. At low penetration of solar and wind, more traditional sources are used in high enough percentages of the total generation so that they can account for these intermittent periods. However, with the urgency of governments and the public to decarbonize their energy systems, these renewable sources are beginning to take a larger role in the generation mix [6] [7].

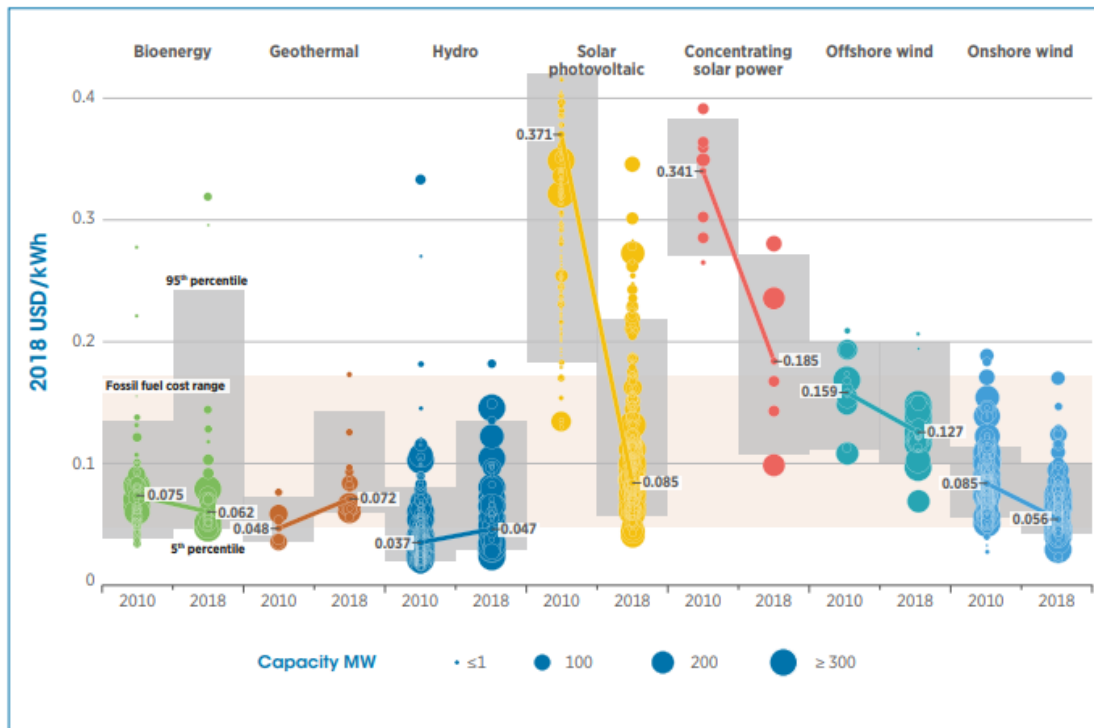


Figure 3.1: Global levelized cost of energy (LCOE) of utility-scale renewable power generation, 2010-2018 [8]

Energy storage systems (ESS) have proved to be a valuable tool which can help to more effectively utilize these generation sources, dispatching this renewable energy when it is most needed rather than simply when it is generated. With added flexibility between time of generation and time of use, the value and dependability of renewable sources is greatly improved. With a variable level of dispatchable energy from ESS, renewable sources can be better positioned economically in the energy market to take advantage of differences between forecasted and real-time generation. In a technical sense, renewable sources are able to reach similar flexibility in dispatch levels as fossil fuel sources, creating a more enticing option for power companies to replace these high-polluting sources.

While energy storage is an important technology with respect to its role in the

integration of renewable sources, it can also be used to provide a wide array of other support services to the energy system. Currently, the energy storage technology with the most globally installed capacity is pumped hydro energy storage (details in next section). These installations are primarily used for electrical energy time shifting (arbitrage) which involves storing energy when marginal prices are low or when renewable generation is higher than demand, and then dispatching this energy during times of high demand and/or high marginal energy price, when it is most needed. Therefore, energy players can purchase low-cost energy to store and then use again when prices have risen due to demand or low renewable generation. Utilizing ESS in this way has been shown to be very economically valuable for power retailers, leading to a significant percentage of annual revenue depending on the area [9].



Figure 3.2: Global Energy storage capacity by Service/Use Case [7]

While most of the world's energy storage capacity in the form of pumped hydro, is being used in this way for energy arbitrage, other emerging ESS technologies are utilized for a more diverse range of applications with regard to the electrical power system as seen in figure 3.2. As discussed above, increasing the dispatchability of re-

newable generation is the second leading utilization of ESS as the technical capacity of these sources are increased and stabilized (renewable capacity firming). Thermal ESS with molten salts or solid materials currently leads in this use as it often supports large concentrating solar power (CSP) plants, increasing reliability of this generation source. Other use-cases for ESS range from transmission/distribution infrastructure services to customer power management and ancillary grid support services. For example, ESS can be used by modern grid controls and power electronics to provide voltage sag compensation, frequency stabilization, and power smoothing on the sec-min timescale. Black start, or powering up a transmission/distribution system after a failure, is possible using stored energy. Additionally, ESS can allow for grid operators to defer the upgrades of transmission or distributing lines that would otherwise be necessary without this added flexibility. Analyzing all of these use-cases of energy storage technologies, the value they play in the current energy system is clear, a role which will only continue to expand in a future system of higher demand and higher renewable penetration [6][10]. In this way, energy storage will be crucial to reach the strongly-forecasted high levels of renewable generation as seen in figure 3.3 .

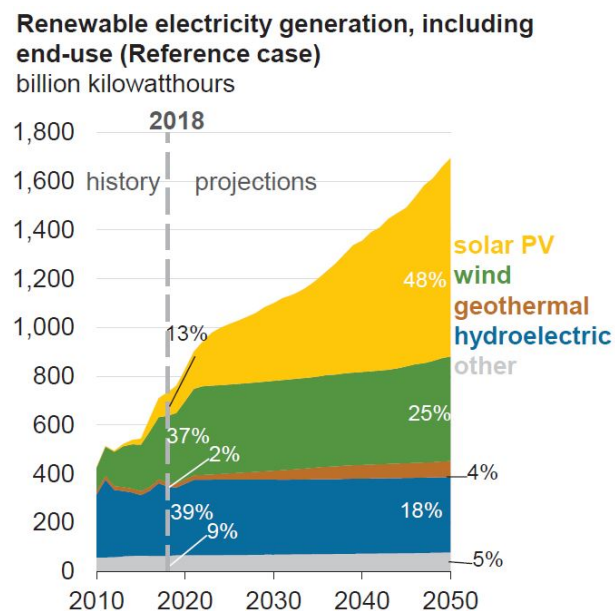


Figure 3.3: Projected growth of United States domestic renewable energy generation [11]

# Chapter 4

## Background

### 4.1 Methods of Grid Energy Storage

As evidenced by the predominant use-cases of various ESS technologies above (figure 3.2), not all technologies are best suited for every application. Different ranges of technical specification are necessary to be useful for certain grid applications as shown in figure 4.1. A further detailed list of power services provided by ESS is presented in figure 4.2. For example, to participate in power quality ancillary services like frequency and voltage support, a storage technology must have agile power dynamics (be able to ramp up or down in very quickly) as necessary for immediate charge or discharge. When a sudden outage or change in generation occurs, these sources must be able to compensate for the effects very quickly to stabilize the frequency. Following a complete outage or shutting down of a power line, ESS solutions can provide black start capabilities, energizing a transmission or distribution line so that it can be used by the power system. On the other hand, to participate in bulk energy services such as peak load shifting (arbitrage), a higher storage capacity and an adequate power to energy ratio while still being economical is required. During this time-shift process, energy is purchased during times of low market price and stored in ESS. This power is then released during times of peak load when it is most needed and also most expensive on the market. A higher capacity is necessary to help shift peak loads as storage systems must provide power for an extended time period. While multiple ESS technologies can be utilized for many of these power services, certain storage technologies are better suited for each based on their mechanical/chemical/or electromagnetic properties [7] [9].

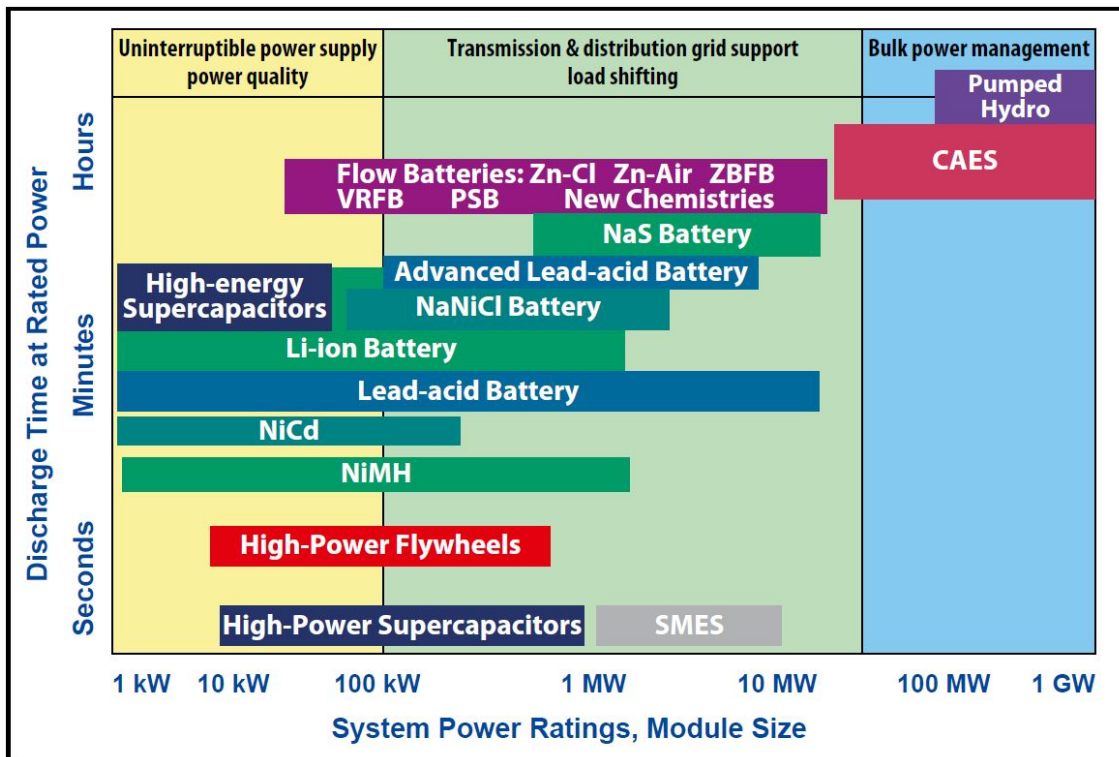


Figure 4.1: Energy storage technologies by discharge time and power ratings showing general use case parameter ranges [7]

Bulk Energy Services		Transmission Infrastructure Services	
Electric Energy Time-Shift (Arbitrage)		Transmission Upgrade Deferral	
Electric Supply Capacity		Transmission Congestion Relief	
Ancillary Services		Distribution Infrastructure Services	
Regulation		Distribution Upgrade Deferral	
Spinning, Non-Spinning and Supplemental Reserves		Voltage Support	
Voltage Support		Customer Energy Management Services	
Black Start		Power Quality	
Other Related Uses		Power Reliability	
		Retail Electric Energy Time-Shift	
		Demand Charge Management	

Figure 4.2: Electricity power system services offered by energy storage technologies [12]

## Pumped Hydro

As the first and only widely-implemented grid storage technology in use today, pumped hydro energy storage involves reservoirs that hold large amounts of water which has been pumped uphill to be released when needed, powering a hydro turbine, as seen in figure 4.3. In 2016, hydro storage contributed to 150 gigawatt (GW) of capacity while all other grid-connected battery storage accounted for only 1.7 GW

[3]. While this capacity is significant comparatively to other storage technologies, pumped hydro has a very limited growth potential due to lack of available/suitable natural areas, environmental impacts of dams, and other issues such as the long-term filling in of reservoirs with sedimentation [13].

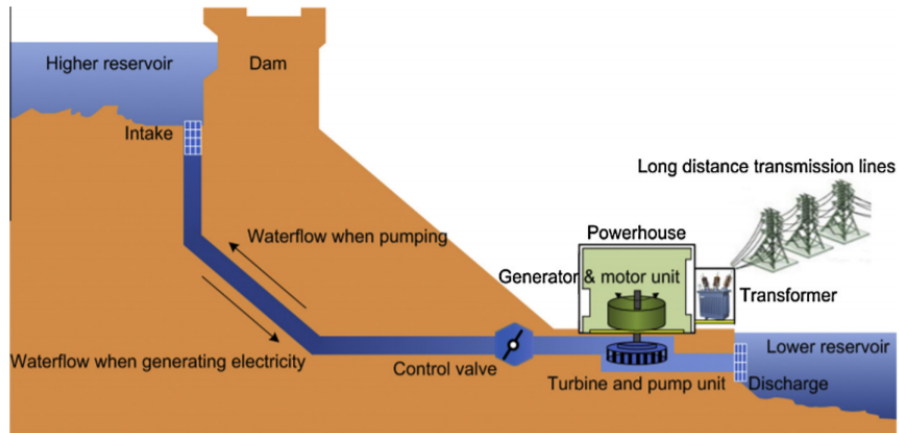


Figure 4.3: Diagram of a pumped hydro plant [14]

### Advantages

- Large capacity systems
- Long lifetime
- Low cost

### Drawbacks

- Intensive public infrastructure required
- Lack of available suitable mountain locations
- Environmental harm of significantly altering natural waterways
- Location usually far from heavy consumption sites, requiring long transport

## Compressed Air

Energy storage in the form of compressed air was first carried out on the grid level in Germany in 1978 with a rated power of 290 megawatt (MW)/900 megawatt-hour (MWh). This technology utilizes large underground caverns into which air is compressed at pressures of 60-80 bar at times of low load. When the energy is needed, the pressure in the cavern is controllably released with natural gas and combusted

in order to power a conventional gas turbine (figure 4.4). While there have been proposed plans for other compressed air energy storage projects throughout the world, many of these projects have run into problems and have not been completed [15] [16]. One project that has been completed however is the ADELE project, also in Germany, which includes a thermal storage system for the generated heat of compression, which can then be later used for the expansion phase. With this added thermal storage, the ADELE system functions as an adiabatic system to reach higher efficiencies [13].

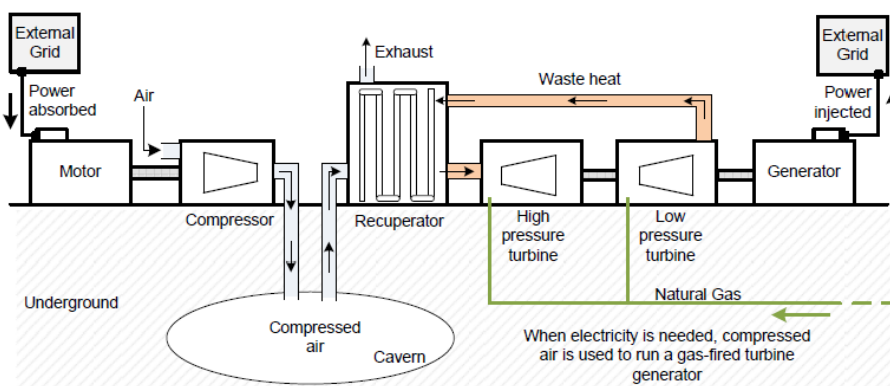


Figure 4.4: Schematic of a compressed air storage plant [16]

## Advantages

- Large capacity, high power
- Infinite air supply to compress

## Drawbacks

- Low availability of suitable natural locations such as porous rocks, aquifers, or empty gas wells

## Thermal

Thermal energy storage has primarily been used in conjunction with large concentrated solar plants as shown in the example of figure 4.5, which use a variety of materials to hold the generated heat so that it can be used at a later time. The three leading materials used for this purpose are high temperature concrete (solid), molten salt (liquid), or a phase change material. Of these three options, solid thermal storage media like high temperature concrete shows the least environmental impact according to a 2012 life cycle assessment (LCA) study [17]. Thermal energy

storage can also be used on a smaller scale for buildings by storing solar heat to be used at night, or even ice storage for summer cooling. These thermal storage systems can be used to significantly reduce energy use of participating buildings [18].

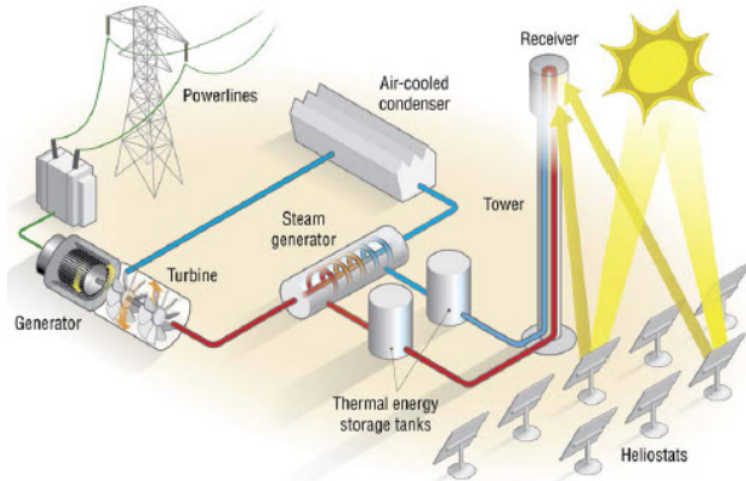


Figure 4.5: Diagram of thermal energy storage system supporting a wind power plant [19]

### Advantages

- Can be used on small or large scale (from residential/commercial buildings to CSP plants)

### Drawbacks

- Suitable for only specific geographical areas with required natural resource (high irradiance or snowfall)

## Superconducting Magnetic

This energy storage technology is based on stored magnetic energy captured in the magnetic field of a direct current (DC) current flowing through a superconducting coil. To reach superconducting properties of large current capability without resistance, the coil (usually niobium or titanium) is cooled to cryogenic temperatures with  $\text{LN}_2$  as seen in figure 4.6. With energy stored in a magnetic field, this technology has the advantage of fast discharge at very high current rates in addition to quick response time. However, maintaining cryogenic temperatures for the superconducting coil requires an intensive energy load [20][16].

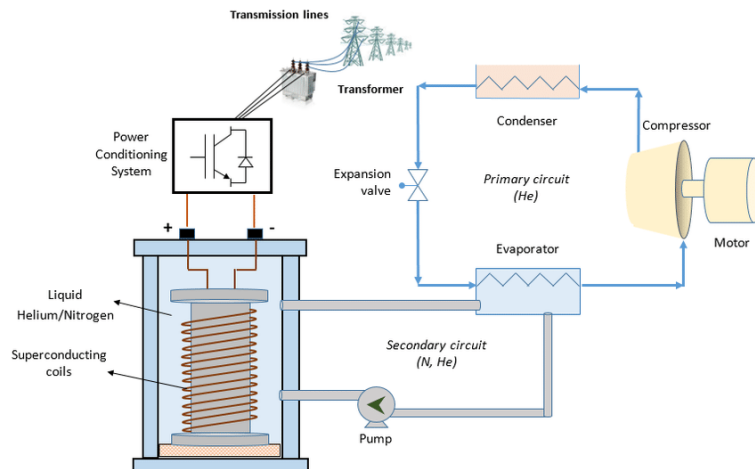


Figure 4.6: Diagram of superconducting magnetic energy storage system [21]

## Advantages

- High discharge power
- Fast response time
- High efficiency ( 90%)

## Drawbacks

- Cryogenic temperatures require energy
- High self-discharge

## Flywheel

Flywheel energy storage utilizes the rotational kinetic energy of a large rotating mass which provides a very responsive source of backup energy (figure 4.7). Magnetic bearings are used to support the rotating mass and reduce mechanical losses while a vacuum is used to reduce wind shear losses. However, as energy is extracted from this source, the discharge time becomes slower as friction becomes a more dominating factor in the rotation of the mass [16] [13].

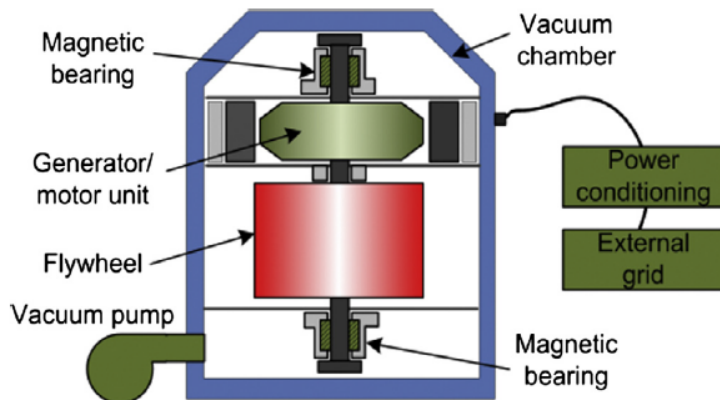


Figure 4.7: Basic diagram of a flywheel energy storage system [7]

### Advantages

- Fast response time
- High discharge power

### Drawbacks

- Discharge power decreases with state of charge (SoC)
- Low energy efficiency

### Capacitor

This energy storage, most commonly double layer supercapacitors, utilize the capacitance formed from the electric double layer at both the anode and cathode of a cell due to the ions of an electrolyte which have magnetically separated to each side as shown in figure 4.8. According to the Helmholtz model, these electrolyte molecules of one charge form a layer on the oppositely charged electrode to create a double layer capacitance. This energy storage technology is often used in support of other power supplies for power quality improvements or power security. It is commonly used in low capacity but high power applications to provide a fast response for a short time [16] [13].

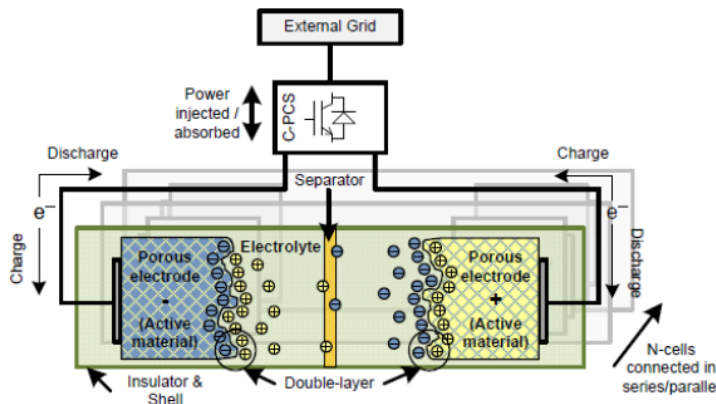


Figure 4.8: Schematic of a supercapacitor cell used for energy storage [14]

## Advantages

- High discharge power and fast response time
- High efficiency
- High power density

## Drawbacks

- Low specific energy
- High self-discharge rates

## Electrochemical

Electrochemical energy storage technologies, or batteries, are the most researched and commercialized of all ESS technologies. This is due to their versatility with respect to portability, discharge power/energy, and range of suitable applications. This storage technology relies on the conversion of electrical energy to electrochemical potential energy through oxidation and reduction reactions at a positive electrode (cathode) and negative electrode (anode) as seen in figure 4.9. Various chemicals are used together based on their unique oxidation and reduction potentials which lead to specific potential differences and influence the cell's electrical characteristics. For example, the nickel-cadmium redox couple produces a nominal potential of 1.3 V while the Li-ion and carbon couple leads to a higher potential of around 3.6 V [16]. In addition, electrochemical batteries can be used to power everything from the smallest of portable electronics to supporting of a large solar PV generation plant.

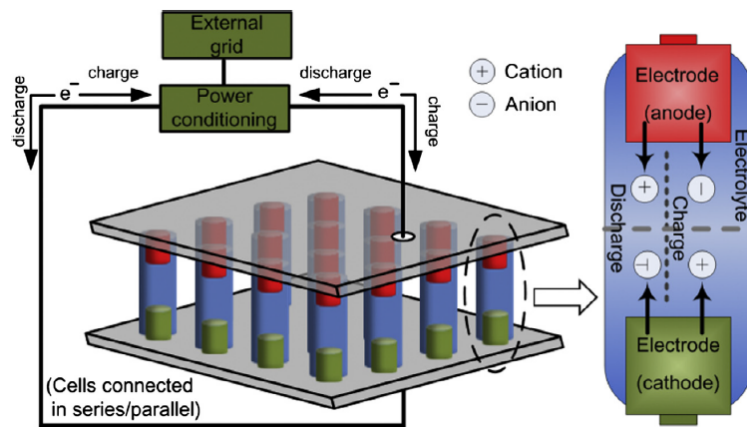


Figure 4.9: Diagram of basic electrochemical cell [14]

### Advantages

- Wide range of electrical characteristics based on specific chemistry
- Simple to integrate, suitable for diverse range of applications
- Versatile, modular and scalable

### Drawbacks

- Most batteries have a low depth of discharge to maintain battery health

## 4.2 Characteristics of Redox Flow Batteries

As mentioned above, within the category of electrochemical energy storage, there exist many chemistries with a wide range of technical features. However, battery voltage is not the only property that can differ between these various chemistries. From figure 4.1, the discharge time and rated power of electrochemical batteries can vary as much between chemistries as they can between separate energy storage categories such as compressed air or mechanical flywheel. Currently, the availability, cost, and safety of these chemicals varies widely throughout these technologies with their own set of advantages and drawbacks.

Redox flow batteries (RFBs), are one of these electrochemical batteries with the potential to play a significant role in the future energy system. As seen in figure 4.10, these batteries feature a liquid electrolyte which flows through two solid electrodes separated by an ion-exchange membrane. The electrolyte can either be the same on both sides or utilize different chemistries as anolyte and catholyte. Two external reservoirs and a pumping system are used to cycle the electrolyte through

the battery cell. During charge or discharge, both oxidation and reduction reactions take place on either side of the cell membrane. On one side, the reduction reaction releases electrons from the electrolyte ions while simultaneously on the opposite side, these electrons are fixed or taken up by the electrolyte ions through oxidation. This electron flow is made possible by charge-carrying ions which pass through the ion-exchange membrane. During charging, the anolyte is reduced, releasing electrons, while the catholyte is oxidized, fixing the electrons in its ions. This leaves an imbalance of charge which is compensated by a flow of cations from the positive to negative side. In this way, a flow of electrons is present in the cell.

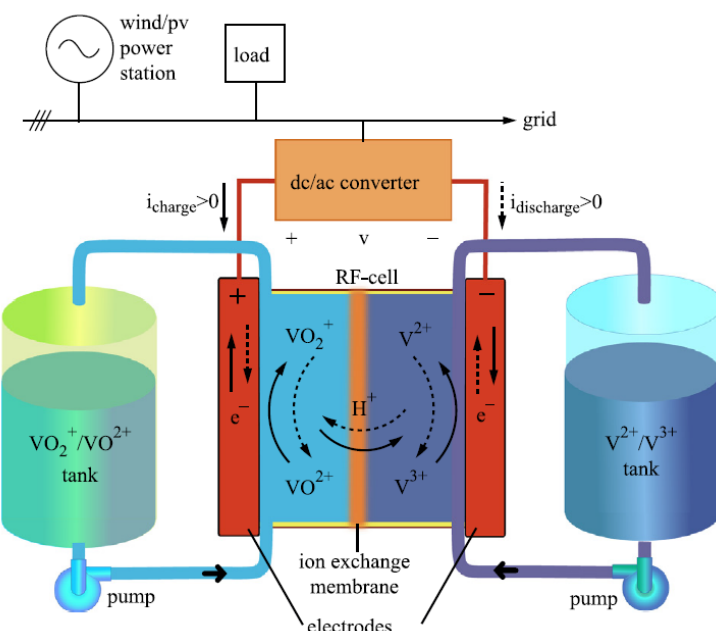


Figure 4.10: Diagram of basic all-vanadium redox flow battery [13]

With this cell function, flow batteries exhibit a unique characteristic which is not found in other electrochemical technologies. By storing a charge in the liquid phase electrolyte which is pumped from a reservoir, the power and stored energy of a RFB are inherently decoupled which allows for customizability and modification of these characteristics, a valuable feature not found in most electrochemical storage technologies. The power rating of a RFB cell is determined by the electrode area while the highly variable energy capacity can be scaled up to the limits of a liquid storage tank for the electrolyte. This ability to easily increase the energy capacity, makes flow batteries especially attractive for large-scale grid support such as peak load shifting as well as support of renewable generation like in the Australian solar plant shown below in figure 4.11 .

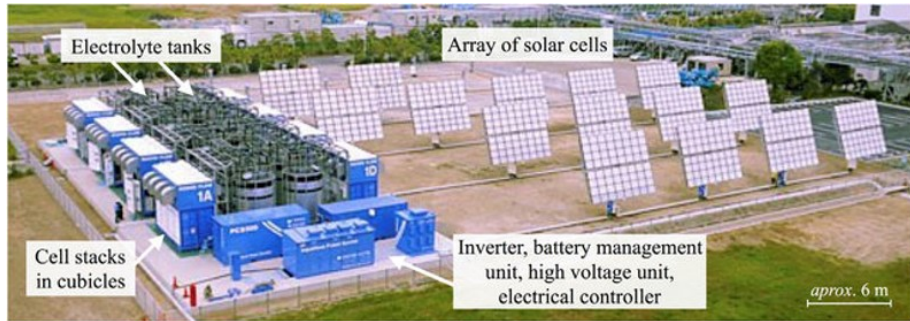


Figure 4.11: Installation of a redox-flow energy storage system supporting the generation of a solar power plant in Australia [22]

In addition to the decoupling of power and energy, RFBs also exhibit a few other specific features which make them a desirable energy storage option. As flow batteries rely on liquid phase chemistry, there is no intercalation or phase change (except for with zinc-based chemistries) during the battery cycling as there is with other electrochemical batteries like lithium-ion. This intercalation process in which a lithium ion inserts itself into the lattice structure of the graphite anode, releasing its stored charge while changing phase from liquid to solid, is a reversible but structurally degrading process. Deformations are easily created in the crystal structure over many cycles which lead to capacity losses. In RFBs, charge-carrying metal ions only change valence state and remain in the liquid phase throughout cycling (or undergo a deposition process in the case of zinc chemistries) and they can therefore be easily cycled many times without degradation. Even with zinc flow batteries, this deposition process is still a more reversible process as deposition occurs only on the surface of the electrode rather than ions inserting within the electrode crystal structure.

Another benefit of RFBs is that throughout cycling, cell temperature is easily controlled due to the high heat capacity of a necessary volume of electrolyte. While heat dissipation can be a challenge for many battery technologies, the constant flow of an electrolyte solution through flow batteries helps to easily maintain a safe and constant working temperature [13].

In addition to these advantages, as liquid electrolyte stores the charge of an RFB, this allows for the potential of rapid recharging by simply replacing this electrolyte, swapping the used electrolyte for previously charged solution. Expanding this feature of flow batteries to the concept of electric vehicles, the possibility for conversion of the conventional petrol station to electrolyte-swapping stations for flow batteries in electric vehicles (EVs) can be viewed as an exciting new frontier for this technology. At the current state of the art for commercial RFBs however, the energy

density is too low to allow for significant driving ranges for cars to run off of these batteries alone. Energy density is based on the electrolyte as it is the active material present in this system. The relation is shown below in equation 4.1 with N number of electrons, C<sub>a</sub> the concentration of active redox species, F Faraday constant, V voltage, and n volume of electrolyte [23].

$$E = \frac{NC_a FV}{n} \quad (4.1)$$

In a more general sense, this characteristic of RFBs is the primary limiting factor for the more widespread use of flow battery technology in other consumer goods. Increasing energy density is a highly-researched subject in this field.

In summary, redox flow batteries are seen to exhibit the following advantages and drawbacks.

### Advantages

- Decoupled power and energy, simple scalability through adjustment of either cell stack design (power) or volume of electrolyte (energy)
- High cycle life due to minimizing phase change of charge carriers
- Simple maintenance of thermal operating conditions

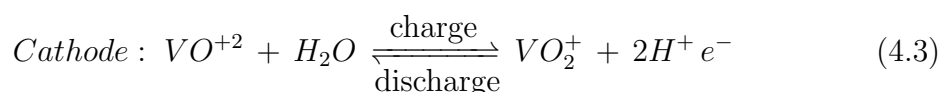
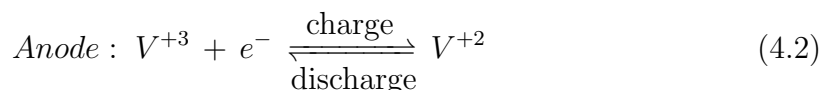
### Disadvantages

- Low energy density and efficiency compared to Li-ion
- Requirement of pumps and flow management systems
- Potential for leakages

## 4.3 Flow Battery State of Art

Since the first redox flow battery was developed by the National Aeronautics and Space Administration (NASA) in the 1970's, many different chemistries have been researched [11]. While this first RFB was based on the iron/chromium (Fe/Cr) redox pair, an all-vanadium as well as a zinc/bromide chemistry have emerged as the primary commercialized flow battery technologies. The all-vanadium chemistry is today the most researched chemistry enjoying the primary benefit of utilizing the

same element in both the anolyte and catholyte, eliminating the possibility of cross-contamination (figure 4.10). Vanadium has the unique property of the capability to form two different redox couples, therefore  $V^{+2}/V^{+3}$  is used in the anolyte while  $VO^{+2}/VO_2^+$  is used in the catholyte. Sulfuric acid is usually used as the solvent for this electrolyte with a vanadium molarity of around 2 M. The half reactions can be seen in equations 4.3 and 4.2 below which produce a theoretical open circuit voltage (OCV) of 1.26 V and a current density of 50-80 mA/cm<sup>2</sup> [13].



While the all-vanadium chemistry has the advantage of no cross contamination, it also has a few disadvantages such as the low solubility of vanadium ions in typical sulfuric acid electrolyte solutions, safety of the sulfuric acid, and the higher cost/low production of raw vanadium. Presently, the total system capital cost of vanadium flow batteries is \$400 per kWh with the primary cost being the electrolyte (55%) [24][25].

### Zinc-Bromine chemistry

The second leading flow battery chemistry which has also enjoyed significant commercialization is the zinc-bromine ( $Zn-Br_2$ ) flow battery of figure 4.12. This is a hybrid battery due to the deposition of metallic zinc ( $Zn^{+2}$  is reduced to Zn) as a thick film on the anode during charge. Meanwhile, on the other side of the membrane, bromide ions are oxidized to bromine ( $Br^-/Br_2$ ).

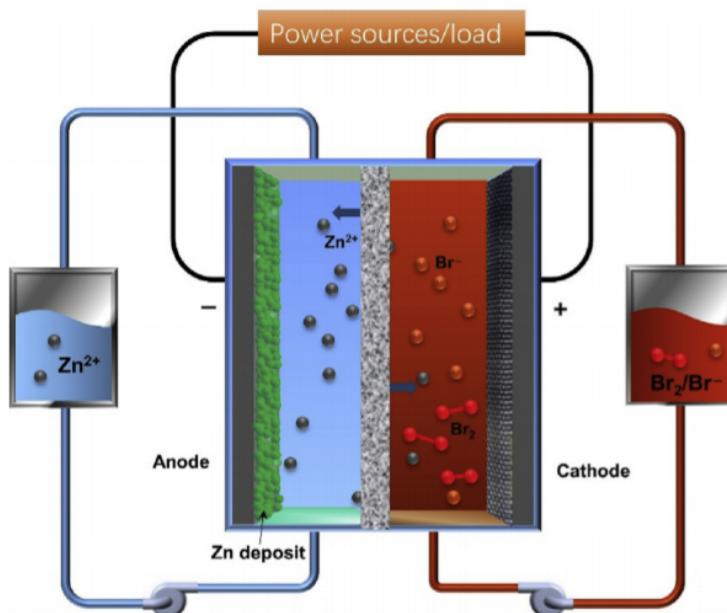
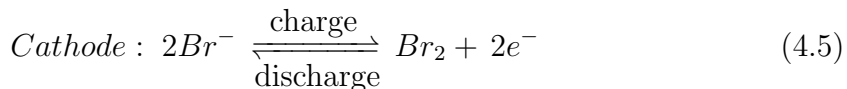
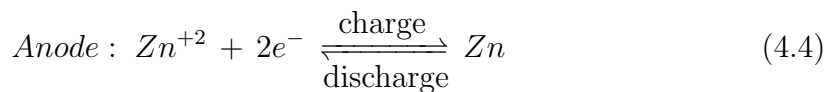


Figure 4.12: Diagram of Zn-Br<sub>2</sub> redox flow battery [26]

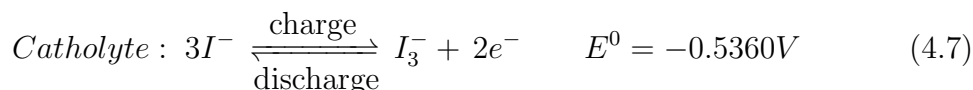
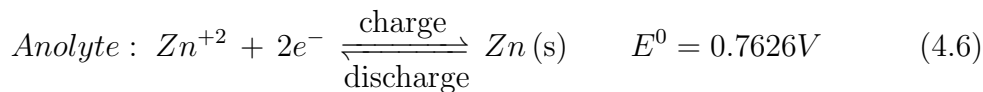
The half cell reactions are shown below in equations 4.4 and 4.5 to produce an overall OCV of 1.82 V.



Zinc-based flow chemistries have the advantage of being very inexpensive and being produced in much higher quantities than vanadium. In addition, the solubility of Zn salts is much higher than vanadium making it possible for higher energy densities. One drawback of Zn-based systems is that they involve the deposition of Zn on the anode rather than the electrolyte remaining in the liquid phase throughout the charge/discharge process. In addition, the bromine element leads to concerns for the ZnBr<sub>2</sub> chemistry as Br<sub>2</sub> is very toxic and corrosive. Throughout charging, Br<sub>2</sub> gases can build up within the battery and cause explosions so it must be complexed (chemically stabilized) with another reagent such as quaternary ammonia [27] [28]. The acidic solution required for this electrolyte further leads to risks with potential contact with users.

## Zinc-Iodine chemistry

To utilize the advantages of zinc-based flow batteries while eliminating many of the issues of bromine, the zinc-iodine ( $\text{ZnI}_2$ ) chemistry was developed. First, iodine is much less toxic than bromine and does not require an acidic solution, making this chemistry much safer.  $\text{ZnI}_2$  has a better solubility (7 M) in aqueous solution than  $\text{ZnBr}_2$  (4 M) which again leads to improvements on theoretical energy density over both  $\text{ZnBr}_2$  and vanadium chemistries. The vapor pressure issue found with  $\text{Br}_2$  gas is also eliminated with the use of  $\text{ZnI}_2$ . Lastly, The  $\text{I}_3^-/\text{I}^-$  redox couple (cathode) is kinetically favorable compared to the  $\text{Br}^-/\text{Br}$  couple leading to the possibility for faster cell dynamics [29]. Meanwhile, the same  $\text{Zn}^{+2}/\text{Zn}$  (s) is used for the anode. Therefore, the half cell reactions become the following, leading to an OCV of 1.3 V:



Using this  $\text{Zn}-\text{I}_2$  chemistry, a high charge density can be produced while utilizing abundant, cheap, and safe chemicals. However, there are a few complications with regard to the  $\text{I}^-/\text{I}_3^-$  redox couple in this chemistry. In the catholyte half cell reaction, iodide ( $\text{I}^-$ ) is the primary charge carrier and often the limiting factor to the charge density of the battery. During charge, this iodide is oxidized to triiodide ( $\text{I}_3^-$ ) as seen in the catholyte equation 4.7 above. However, in the system described above, it is clear that for every 3 moles of  $\text{I}^-$ , only 2 moles of  $e^-$  are produced. Therefore only 2/3 of iodide ions are contributing to the battery energy density. Because of this, the theoretical energy density of any system utilizing the  $\text{I}^-/\text{I}_3^-$  is limited as only 67% of free  $\text{I}^-$  moles can be utilized for charge transfer. Additionally, the solubility of  $\text{I}_2$  is low in aqueous solution, which can further limit the formation of necessary  $\text{I}^-$  or  $\text{I}_3^-$  ions for charge transfer.

One approach to this issue is to introduce bromide ions ( $\text{Br}^-$ ) again to the system to increase the solubility of iodine, forming  $\text{I}_2\text{Br}^-$  which keeps  $\text{I}^-$  free to contribute to the total energy density of the system 4.13. This approach proved effective and in early 2017, the highest experimental energy density (at the time) for an aqueous flow battery was achieved at 101 Wh/L<sub>pos+neg</sub> [30]. However, introducing bromide again brought up the same toxicity issues which were trying to be avoided by switching to the I-based anolyte.

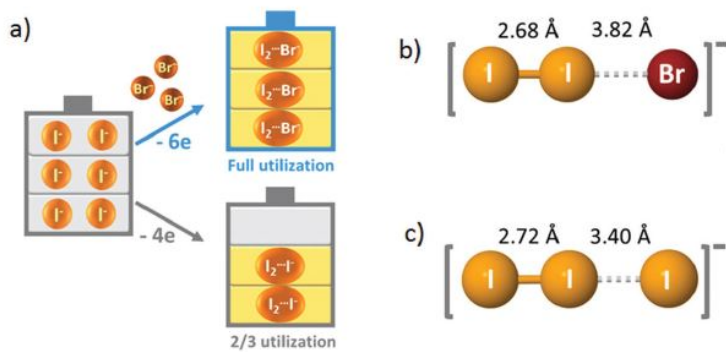
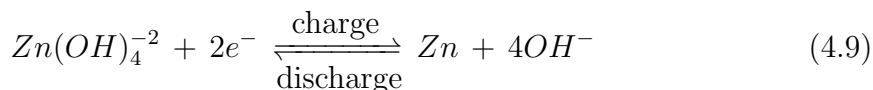


Figure 4.13: a) Graphical representation of the complexing of iodine ( $I_2$ ) by bromide ions ( $Br^-$ ). The structure of  $I_2Br^-$  and  $I_3^-$  ions are also shown in b) and c) [30]

Another approach to unlocking this extra capacity of the  $I^-/I_3^-$  couple through much less toxic chemicals is by the addition of potassium iodide (KI). KI produces free  $I^-$  ions in solution which greatly increase the solubility of  $I_2$  by equation 4.7 below. The potassium also has an additional benefit of acting as a free charge carrier, moving back and forth between the Nafion (cation-exchange) membrane during charge and discharge to maintain the charge balance between anolyte and catholyte [31] [32].



Another development which has been shown to be used concurrently with the addition of KI above, is the use of zincate ( $Zn(OH)_4^{2-}$ ) rather than ZnI<sub>2</sub> which tunes the pH level of the electrolyte in turn, significantly increasing the redox potential of the Zn redox pair (+0.497 V) [31]. With this addition of zincate, the catholyte equation then becomes the following:



With the above alkaline environment and a catholyte concentration of 6M, this team was able to reach a very high energy density of 330.5 Wh/L<sub>cath</sub> (at a 44 % depth of discharge for 10 cycles) [31]. While there is still room for improvement, this chemistry has been proven to show excellent, state of the art energy density.

## 4.4 Electrochemical Impedance Spectroscopy

While advances in flow battery technologies are progressed, essential characterization techniques are utilized which are crucial in achieving a technical under-

standing of fundamental electrochemical processes which effect cell performance. Microscopy methods such as scanning electron microscopy (SEM) and transmission electron microscopy (TEM) are often used to analyze the microstructure of electrodes *ex situ*, while methods like nuclear magnetic resonance (NMR) and X-ray diffraction (XRD) are used for compositional analysis to understand what materials or chemicals are reacting in a system. Over the past few years, many *in situ* characterization methods have been developed as well which provide a valuable understanding of the cell during cycling such as differential electrochemical mass spectroscopy (DEMS) and synchrotron-based XRD [33]. Spectroscopy methods such as UV-Vis typically used to analyze changes in flow battery electrolytes. On a device level, cycling evaluations like cyclic voltammetry or charge-discharge analysis can reveal redox potentials and cell performance parameters like voltaic and coulombic efficiencies [34].

One of these device level characterization methods is Electrochemical Impedance Spectroscopy (EIS). This analysis tool is used to model some of the fundamental parameters of a battery cell by applying either a small galvanostatic input current (GEIS) and measuring the output voltage, or small potentiostatic input voltage and measuring the output current (PEIS). With the resulting impedance response, several phenomena that occur at different time scales depending on the applied frequency, can be discerned [35].

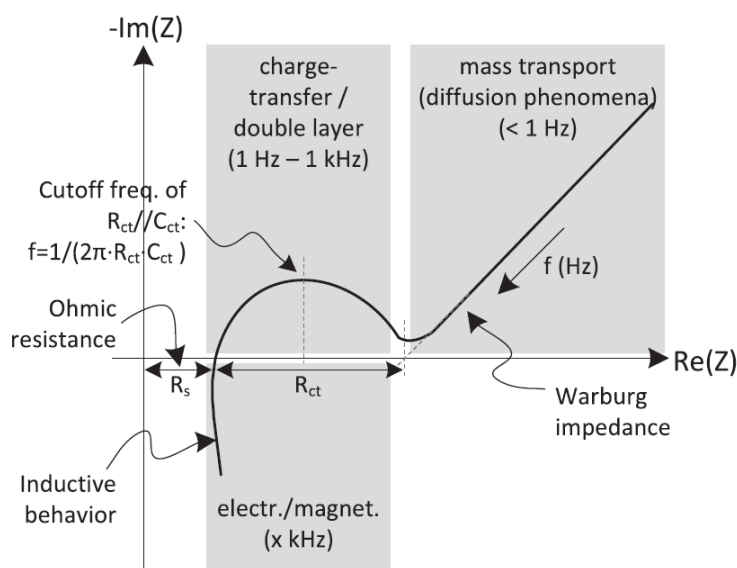


Figure 4.14: Characteristic Nyquist curve for an electrochemical battery cell displaying the general curve attributes [16]

In the study of flow battery systems, PEIS is used more often as it is more likely

to utilize the full frequency range of the potentiostat whereas GEIS is typically used in the low frequency region. Because of this, GEIS is used for systems with slower kinetics in which this low frequency region is more important [36]. With PEIS, the cell is subjected to small alternating current (AC) voltage perturbations (ex: 100 mV) ranging from hundreds Hz-MHz range while the resulting phase shift of the AC current is measured. From figure 4.14, first the internal (ohmic) resistance of the cell is shown as  $R_s$  along the real axis. For redox flow batteries, this resistance can be attributed to ionic exchange resistance of the membrane, electrolyte solution resistances, contact resistances and electrode resistances. Often, the membrane resistance is a dominating factor for  $R_s$ . This ohmic resistance can be calculated using the resistivity ( $\rho$ ), thickness between electrodes (d), and electrode area (A) of a solid material or the mobility ( $\mu$ ) and concentration ( $C_i$ ) for an aqueous solution as seen in the equations 4.10 and 4.11 below.

$$R_{ohm} = \rho \frac{d}{A} \quad (4.10)$$

$$R_{solution} = \frac{1}{\sum z_i u_i C_i} \quad (4.11)$$

For flow batteries using porous carbon felt electrodes, this resistance can also include a distributed resistance component in parallel, which overlaps the following charge transfer region of figure 4.14, seen as a small linear portion. This resistance is due to the parallel ionic resistance of the electrolyte as well as the ohmic resistance of the electrode within the carbon felt seen in figure 4.15 [35].

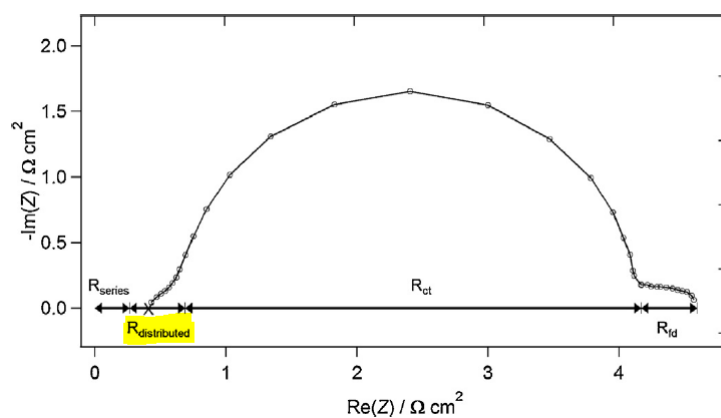


Figure 4.15: Nyquist plot of an all-vanadium battery showing distributed resistance in the high-frequency region [37]

Moving to the right of the Nyquist plot, decreasing in applied frequency, a semi-circle region begins to appear following the small distributed resistance portion. The

real impedance portion of this region corresponds to the charge transfer within the cell, which arises from electrochemical reactions between electrode and electrolyte, as well as the electric potential and chemical gradients that occur between the interface and bulk electrolyte which all together contribute to this transfer of charge . This is referred to as the charge transfer resistance ( $R_{ct}$ ) and it can be expressed below by the Butler-Volmer relationship with a high dependence on electrochemical potential [35].

$$R_{ct} = \frac{R_G T}{z F i_o} \quad (4.12)$$

In this relation,  $R_G$  represents the gas constant,  $T$ - temperature,  $z$ - number of electrons, and  $i_o$ - exchange current density.

Usually shown in parallel with  $R_{ct}$ , a double-layer capacitance component ( $C_{dl}$ ) contributes to the reactance portion in the imaginary impedance axis of the semi-circle shape. This double layer is formed at the electrode/electrolyte interface from a buildup of charge carrier ions. As these ions transfer their charge to the electrode, a potential drop occurs between this buildup of ions and the next layer, referred to as the inner and outer Helmholtz planes shown in figure 4.16. This capacitance can be made up of both this Helmholtz contribution as well as a diffusion layer contribution which arises from the concentration gradient of ions between the interfacial area and the electrolyte bulk. Therefore, this diffusion layer component of  $C_{dl}$  increases for larger applied voltages or concentrations. In this work, a voltage of only 10 mV and concentrations of 1.5 M are used so this Helmholtz capacitance can be disregarded. The double layer capacitance then becomes equal to the Helmholtz component below with permittivity  $\epsilon$ , vacuum permittivity  $\epsilon_0$ , and Helmholtz layer thickness  $L_H$  (usually around 1-2 nanometers).

$$C_{dl} = \frac{\epsilon \epsilon_0}{L_H} \quad (4.13)$$

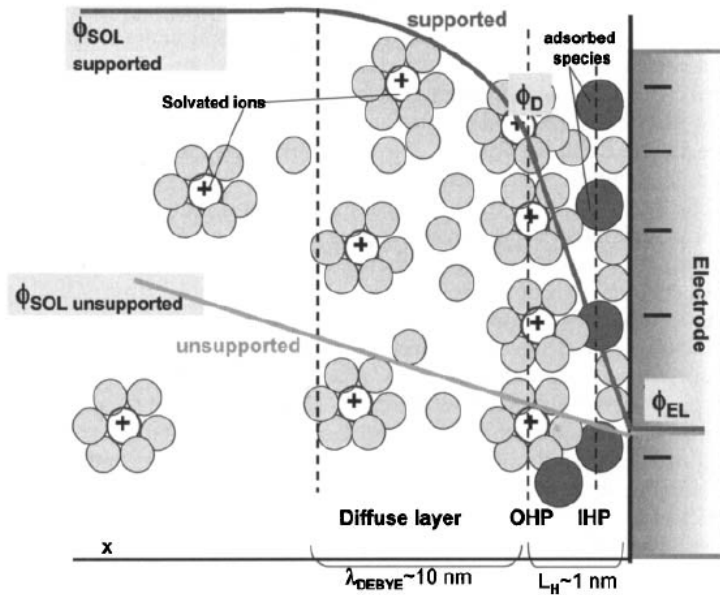


Figure 4.16: Diagram of Electrode/electrolyte interface showing the buildup of ions at the inner and outer Helmholtz planes (IHP and OHP respectively) which lead to a potential drop and the formation of a double layer capacitance  $C_{dl}$  [35]

Finally, the Warburg impedance  $Z_w$  can be found from the slope of the linear section in the low frequency region. This value corresponds to the contribution of diffusion of charge-carrying ions, only occurring at low enough frequencies to facilitate ion movement through the cell electrodes [35].

# Chapter 5

## Objectives and Scope

The purpose of this thesis work is to first, design and assemble an effective ZnI<sub>2</sub> redox flow battery and second, to use the analysis method of electrochemical impedance spectroscopy to better understand the functioning of this flow battery. Through a deeper fundamental understanding of the electrochemical kinetics of the flow cell, I hope to find areas for further improvement of cell performance.

In this study, I focus on the ZnI<sub>2</sub> redox flow chemistry. With many different redox flow battery chemistries currently being researched, it was decided to study the ZnI<sub>2</sub> system in aqueous solution for a few important reasons.

1. Improvements compared to ZnBr<sub>2</sub>: zinc and iodine are both very abundant, non-toxic, and inexpensive, giving them a high potential for commercial use in redox-flow batteries. Iodine was used specifically instead of bromine for its environmentally-safe properties, increased solubility in aqueous solution, and because it does not require an acidic solvent. In addition, the iodide/triiodide redox pair has faster cell dynamics than the bromide couple [29].
2. The voltage range of the redox potentials was strategically chosen in order to be used in conjunction with solar cells which are currently being developed in this lab group.
3. A growing amount of research is currently being published on this chemistry, continuously making improvements on cell performance and proving this chemistry to be an important player in the flow battery field [29] [38] [28] [39] [30] [31].

Although the amount of research being published in the area of ZnI<sub>2</sub> flow batteries is increasing, the number of studies involving this chemistry, or flow battery chemistries in general, is significantly lower than those in lithium-ion batteries, which are much more commercially available today due to their high energy density and effective performance. As the energy density of redox flow batteries is much lower, this technology have not been able to reach the same levels of commercial success with only a few companies currently producing them. Of the roughly 1.9 GW of installed electrochemical storage systems worldwide in 2017, 59% was lithium-ion and only 2% included flow battery technology [7]. The studies involving electrochemical impedance spectroscopy of ZnI<sub>2</sub> chemistry is much lower than the published articles on EIS of Li-ion batteries. Of the 91,533 currently published articles on Li-ion chemistry, 13,923 articles (15%) involve electrochemical impedance spectroscopy. However, of the only 2,626 works on ZnI<sub>2</sub>, only 20 (>1%) concern impedance studies of this chemistry, evidence of the need for more information on this area of this emerging technology [40].

# Chapter 6

## Experimental Methodology

### 6.1 Electrochemical Cell Configuration

A Microflow<sup>TM</sup> cell by Electro cell<sup>®</sup> was used to build the full cell setup as seen in figures 6.1 and 6.2. Viton<sup>TM</sup> gaskets (1 mm thickness) were used on the outer edges of the current collector in contact with polytetrafluoroethylene (PTFE) separator plates. A titanium current collector was used on the negative side to hold the electrode. For the anode, graphite foil (0.5 mm thickness, Alfa Aesar<sup>®</sup>) was used in contact with a 10 cm<sup>2</sup> square of thin carbon felt (1.5 mm thickness, Sigracell<sup>®</sup> GFA 1.5 FA) with four Ti wires inserted in a crosshatch pattern as seen in full cell diagram 6.1. A Viton<sup>TM</sup> gasket (3 mm thickness) was cut in order to insert a AgCl/Ag reference electrode in the negative side of the cell. A Nafion<sup>TM</sup> 117 membrane was used between the cell compartments, held in place with Viton<sup>TM</sup> gaskets with an opening of 10 cm<sup>2</sup>. For the cathode, a 10 cm<sup>2</sup> square of thermally treated thick carbon felt (6 mm thickness, Sigracell<sup>®</sup> GFA 6EA) was used in contact with a graphite current collector.

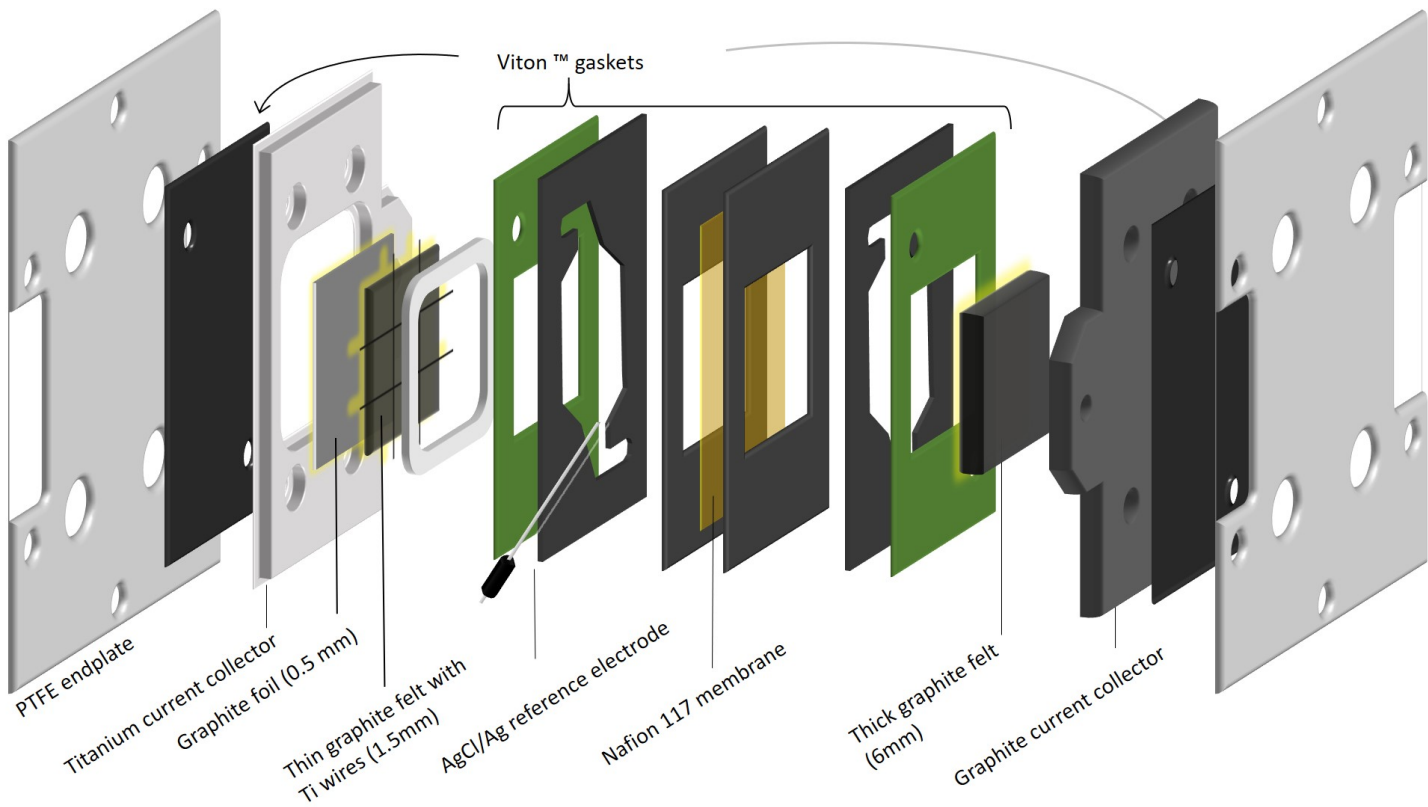


Figure 6.1: Diagram of full cell components (not to scale)

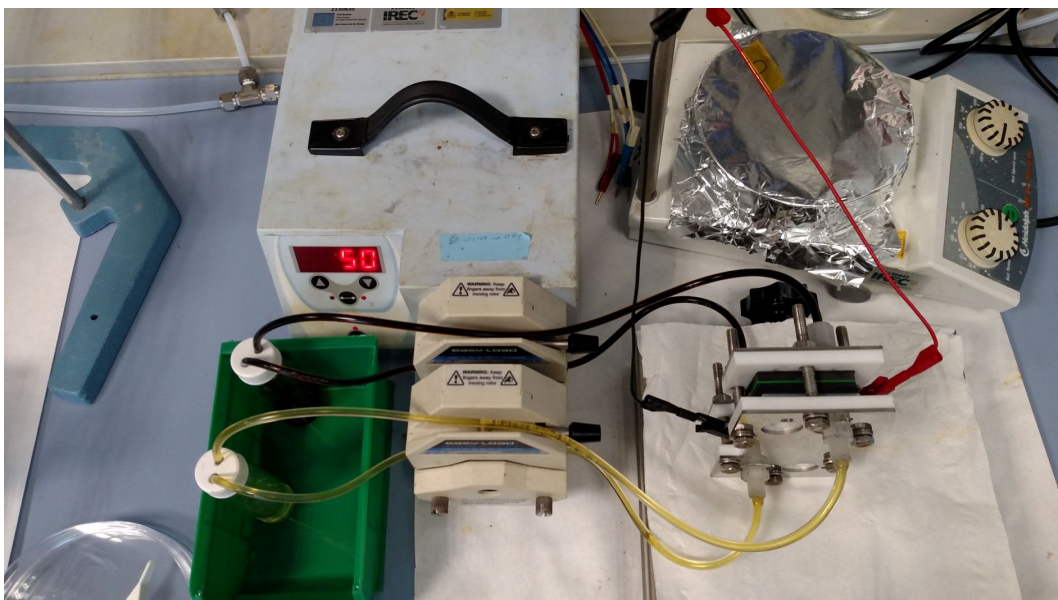


Figure 6.2: Full cell setup with peristaltic pump and electrolyte reservoir vials

Thermal treatment of both thick and thin carbon felt electrodes was done at 420 °C for 10 hours using a ramp rate of 5 °C/min. A 1.5 M aqueous solution of ZnI<sub>2</sub> was prepared and mixed with 1.5 M KI solution to make 10 mL of electrolyte solution for the both the catholyte and anolyte reservoirs (figure 6.3).



Figure 6.3: Vial of  $1.5 \text{ M } \text{ZnI}_2 + 1.5 \text{ M } \text{KI}$  electrolyte solution

Two separate external impedance cells were built as shown in figures 6.4 and 6.5 as done in [27]. These identical cells consisted of a working electrode (cathode) and counter/reference electrode (anode) without a separating membrane. Graphite foil as used for the full cell (0.5 mm thickness, Alfa Aesar<sup>®</sup>) was used for the cathode. Thin carbon felt (1.5 mm thickness, Sigracell<sup>®</sup> GFA 1.5 FA) was used as the anode. Graphite current collectors with serpentine flow paths were used however, small Viton<sup>™</sup> pieces were used as seen in figure 6.6 in order to block off the extra flow channels of the cell, thereby creating a single flow-through cell design. The end connections of the unused channels were also sealed using a thermoplastic hot-melt adhesive in order to guarantee a seal on these outlets.

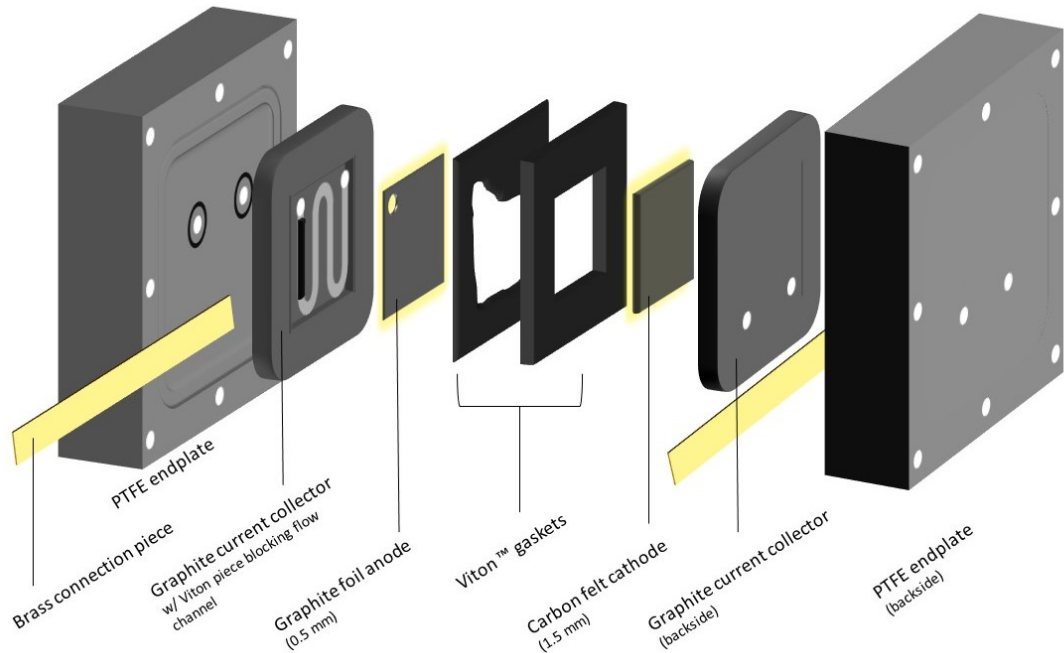


Figure 6.4: Diagram of impedance cell components (not to scale). Note: Only one opening was used on each side while the other was blocked using Viton™ blocking piece on graphite current collector as seen below in fig.6.6. This way a single flow-through design was achieved.

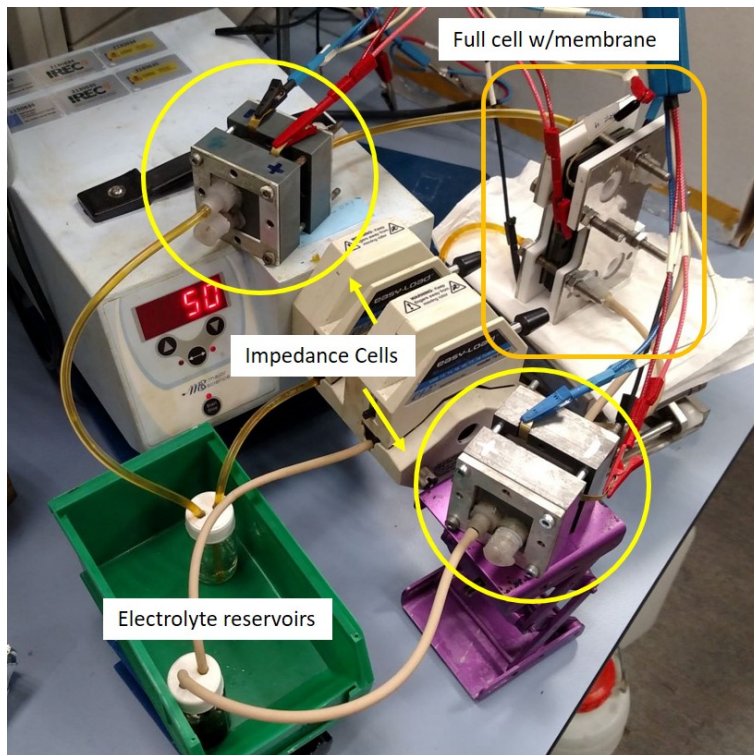


Figure 6.5: Full cell with impedance cells setup with peristaltic pump and electrolyte reservoir vials



Figure 6.6: Current collectors of impedance cells showing Viton<sup>TM</sup> gaskets used to help block flow channel and create flow through design

Tygon<sup>TM</sup> tubing was used in both the full cell setup and full cell with impedance cell setup to connect the cells to the electrolyte reservoirs. A peristaltic pump was used for both channels with a flow rate of 13 mL/min. Two glass vials with holes in the caps were used as electrolyte reservoirs.

A Bio-Logic<sup>®</sup> VMP3 potentiostat was used for all experiments. Three channels were utilized; one to measure EIS for each impedance cell and another to control charge and discharge for the full cell setup as seen in figure 6.5.

The peristaltic pump was set to a flow rate of 13 mL/min to produce a small dripping flow in each electrolyte reservoir. EIS was run in potentiostatic mode with a voltage of 10 mV through the frequency range from 200 kHz-100 mHz. Charging was done at a current of 100 mA up to 67% SoC corresponding to a theoretical capacity of 536 mAh.

# Chapter 7

## Results and Discussion

### 7.1 Characterization of Full Cell

#### Electrodes

Carbon paper and calcinated carbon felt which were used for electrodes of both the full and impedance cells. Thermal treatment was performed on the carbon felt to activate the surface of the carbon fibers, making them more hydrophilic. In this way, the fibers allow for better contact with the aqueous electrolyte solution, leading to adequate charge transfer.

SEM images of figures 7.1 and 7.2 show the porous surface of the electrodes which facilitates the electrochemical reactions.

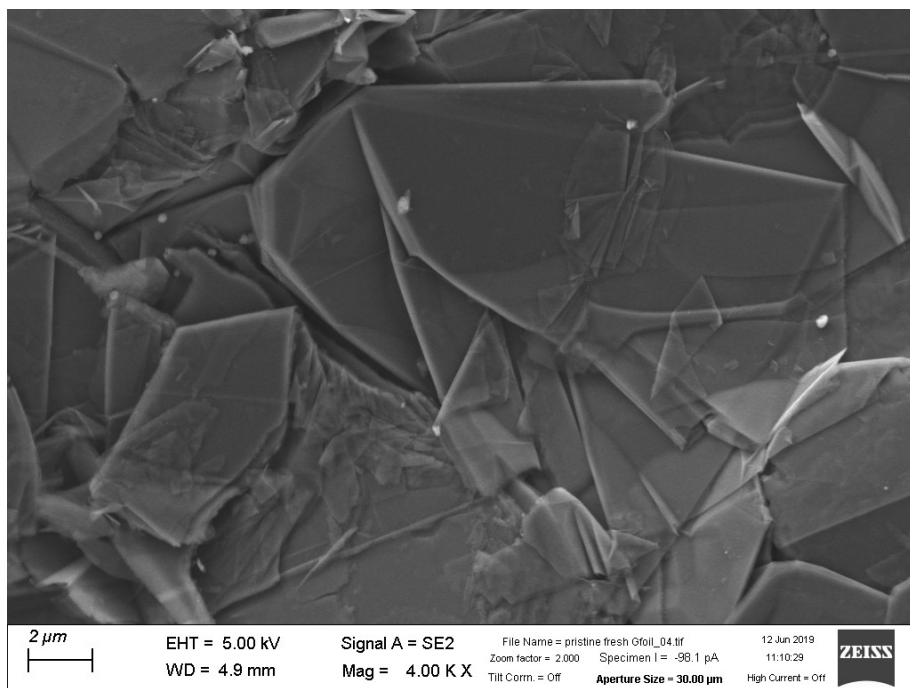


Figure 7.1: SEM image of graphite foil used for anode of impedance cells [41]

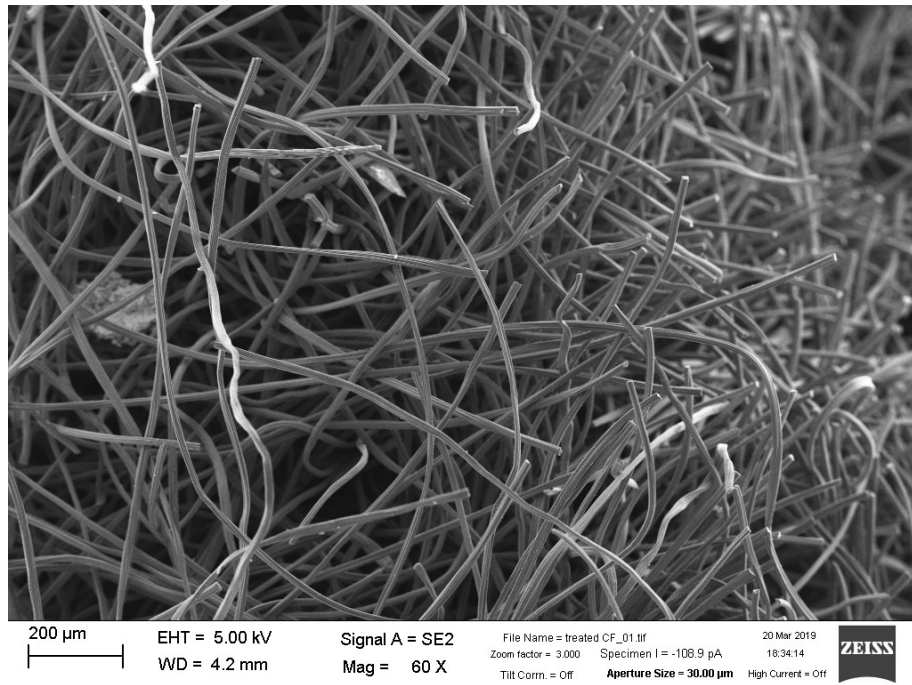


Figure 7.2: SEM images of thermally-treated carbon felt for cathode and anode of full cell as well as cathode of impedance cells [41]

After cycling, metallic zinc is deposited on the anode surface of the full cell. SEM was used to analyze the morphology of this deposition layer as seen in figures 7.3 and 7.4.

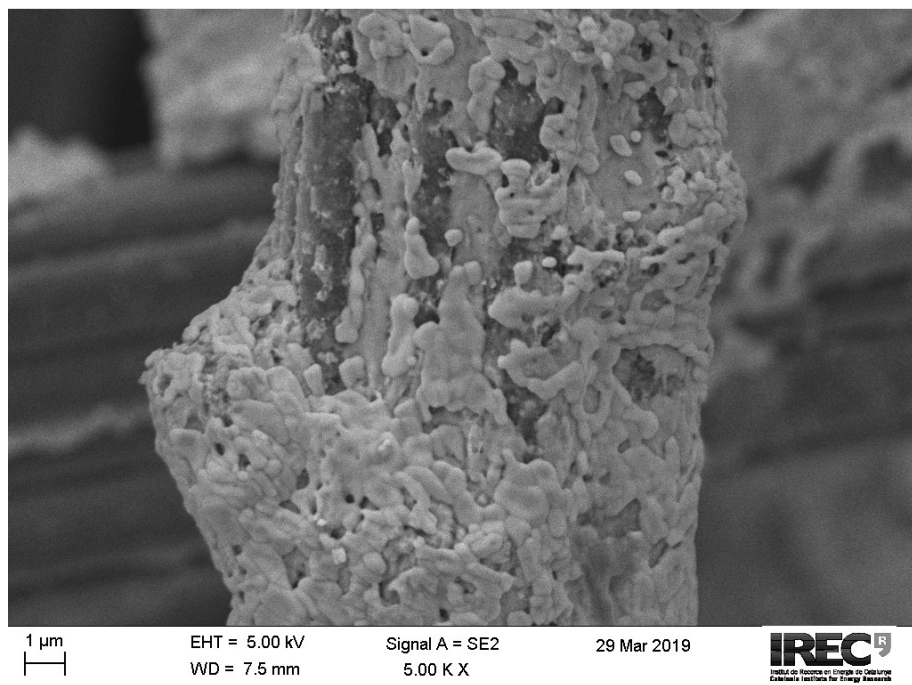


Figure 7.3: SEM image of metallic zinc deposit on carbon felt anode single fiber [41]

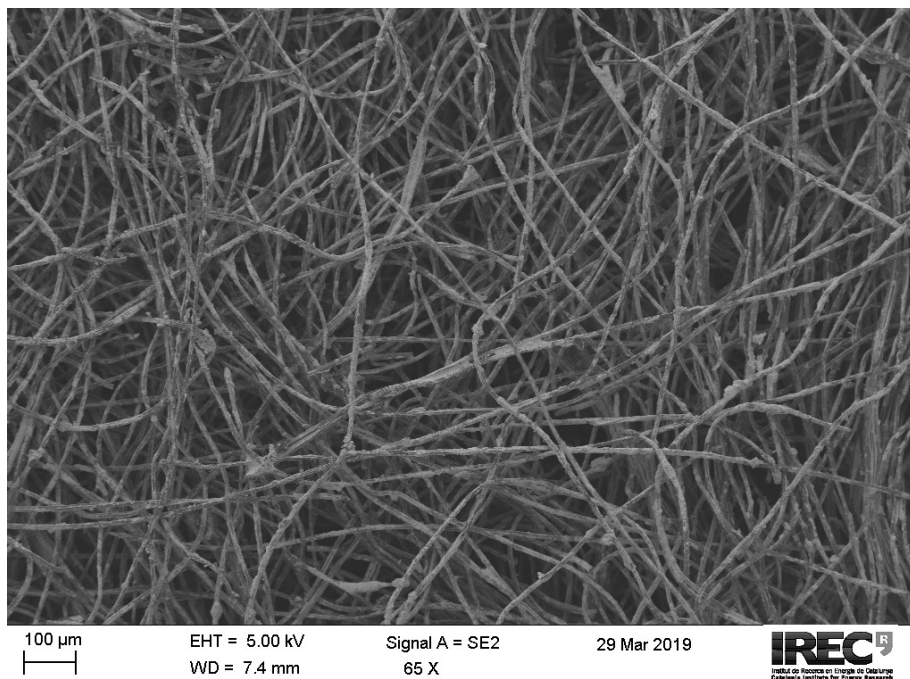


Figure 7.4: SEM images of metallic zinc deposit on carbon felt anode bulk after cycling [41]

## Basic Cell Parameters

In order to characterize our cell, a few basic battery parameters were first defined. The stored charge or capacity (Q), is defined as delivered current over a specified time period and is often given in units of ampere-hours [Ah] or milli-ampere hours [mAh]. The strength of this charge or the power (P) of the cell is current times the potential of the battery in units of watts [W]. 1 watt is the equivalent of 1 volt times 1 amp. Next, the measure of the stored strength of the battery or energy, calculated as the capacity times the voltage in watt-hours [Wh]. To understand how much power or energy a certain battery contains per unit weight, the power and energy density are required, given in [W/kg] and [Wh/kg] respectively. These are all important parameters which are commonly used to judge the performance of a battery.

## Determination of Charge Density

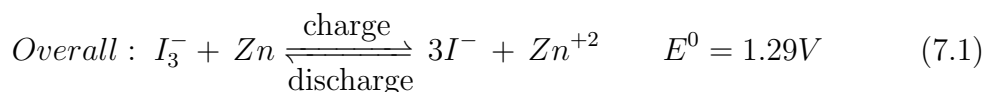
Calculating the energy density of this electrolyte, focus is paid to the active redox couples and their contribution of generated electrons. Energy density is defined in terms of dimensional analysis shown in equations below can be used to calculate generated electrons with Faraday's constant of 96485 Coulomb/mol e<sup>-</sup>.

As explained above in the background section, an aqueous solution of 1.5 M of

$\text{ZnI}_2$  and 1.5 M of KI was used in this study. This electrolyte is shown in figure 6.3. According to equations 4.6 and 4.7, the redox pairs of  $\text{Zn}^{+2}/\text{Zn}$  and  $\text{I}^-/\text{I}_3^-$  were utilized for the cathode and anode respectively as seen in the full cell schematic of figure 7.5. KI and  $\text{ZnI}_2$  both served the dual purpose of contributing  $\text{I}^-$  ions as well as  $\text{K}^+$  or  $\text{Zn}^{+2}$  ions to serve as free charge carriers moving back and forth across the membrane, balancing the charge between anolyte and catholyte throughout the charge/discharge process. In this way, KI and  $\text{ZnI}_2$  act as bifunctional salts in this system.

The cell was charged to 67% SoC (536 mAh) based on the ionic charge balance after analyzing the capacity contributions from both redox couples. It was found that the formation of unwanted solid  $\text{I}_2$  becomes thermodynamically favorable over formation of  $\text{I}_3^-$  at low concentrations of  $\text{I}^-$  in the system (equation 4.8). This solid  $\text{I}_2$  does not contribute to the  $\text{I}^-/\text{I}_3^-$  redox pair and is not a charge carrier, leading only to a decrease in charge capacity of the system. To avoid this  $\text{I}_2$  formation, the cell was cycled to a maximum of 67% SoC to maintain solubility of the catholyte.

To then solve for the charge capacity of the full cell, the capacity of the active charge carriers of the redox pairs must be determined for this system. First, the capacity of the  $\text{Zn}^{+2}/\text{Zn}$  redox couple is calculated. For this redox pair, only the  $\text{ZnI}_2$  contributes to these charge carriers so only this salt is used to calculate the capacity in the dimensional analysis of 7.2. Therefore, from equation 7.1 below of the overall cell reaction, and the dimensional analysis calculation of equation 7.2, for every mol of  $\text{Zn}^{+2}$ , 2 mols of electrons are produced, leading to a theoretical capacity of 804 mAh. On the other hand, when calculating the capacity contribution from the  $\text{I}^-/\text{I}_3^-$  redox pair, both salts ( $\text{ZnI}_2$  and KI) contribute to this charge carrier and must be considered. From the contribution from both  $\text{Zn}^{+2}$  and KI salts, 4.5 mols of  $\text{I}^-$  are produced. It is then shown that for every 3 moles of  $\text{I}^-$ , 2 moles of  $\text{e}^-$  are produced, which leads to the same theoretical capacity of 804 mAh as the  $\text{Zn}^{+2}/\text{Zn}$  redox couple.



**Zn<sup>+2</sup> capacity contribution**

$$\frac{10 \text{ ml electrolyte} \cdot 1 \text{ L}}{1000 \text{ ml}} \frac{1.5 \text{ M ZnI}_2}{1 \text{ L}} \frac{1 \text{ mol Zn}^{+2}}{1 \text{ mol ZnI}_2} \frac{2 \text{ e}^-}{1 \text{ mol Zn}^{+2}} \frac{96485 \text{ C}}{1 \text{ mol e}^-} \frac{1 \text{ A} \cdot \text{sec}}{1 \text{ C}} \frac{1 \text{ hr}}{3600 \text{ sec}} \cdot 100 = 804 \text{ mAh}$$
(7.2)

**I<sup>-</sup> capacity calculation**

$$\frac{10 \text{ ml electrolyte} \cdot 1 \text{ L}}{1000 \text{ ml}} \frac{1.5 \text{ M ZnI}_2 + 1.5 \text{ M KI}}{1 \text{ L}} \frac{2 \text{ mol I}^-}{1 \text{ mol ZnI}_2} \frac{1 \text{ mol I}^-}{1 \text{ mol KI}} \frac{2 \text{ e}^-}{3 \text{ mol I}^-} \frac{96485 \text{ C}}{1 \text{ mol e}^-} \frac{1 \text{ A} \cdot \text{sec}}{1 \text{ C}} \frac{1 \text{ hr}}{3600 \text{ sec}} \cdot 100 = 804 \text{ mAh}$$
(7.3)

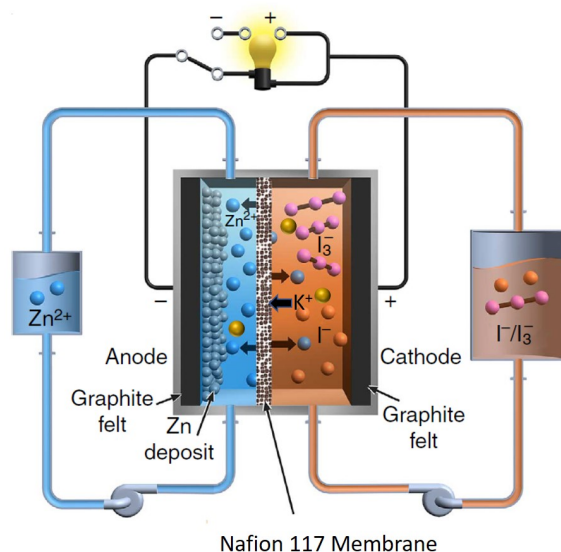


Figure 7.5: Schematic of full cell setup used in this study [28]

**Charge-Discharge Analysis**

To characterize the voltage, coulombic and energy efficiencies of the system (VE, CE, and EE respectively), the full cell was charged and discharged through its full capacity. From this data, the potential versus capacity of the battery was plotted as seen in 7.6. The average discharge voltage over the average charge voltage of figure 7.6 gives VE (equation 7.4). Coulombic efficiency (CE) was determined by

calculating the area below the charge-discharge curve and thereby integrating the voltage over capacity curve. Finally, calculation of energy efficiency was done by multiplying VE and CE in equation 7.6 [42].

$$VE = \frac{\text{average discharge voltage}}{\text{average charge voltage}} \quad (7.4)$$

$$CE = \frac{\text{discharge capacity}}{\text{charge capacity}} \quad (7.5)$$

$$EE = VE \cdot CE \quad (7.6)$$

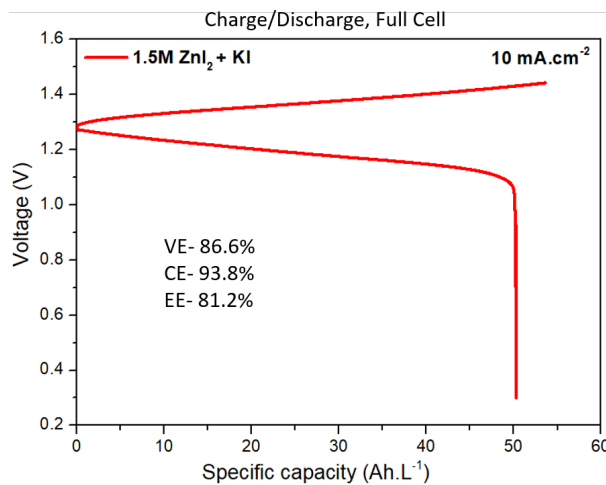


Figure 7.6: Charge/discharge analysis of full cell setup with Voltage, Coulombic, and Energy efficiencies [41]

## 7.2 Impedance Results

### Full Cell

Impedance curves were first obtained from the full cell setup at various SoC's. In figure 7.7, the cell was measured at 0% SoC before charging to 67% (536 mAh) for two cycles. All EIS parameters (ohmic resistance, charge-transfer resistance, and the diffusion coefficient) all decrease upon charging as seen from the much shorter red and dark green traces of 67% SoC. This is due to the higher potential of the battery at fully charged (67%) compared to the 0% SoC which makes the discharge more thermodynamically favorable. The kinetics of a chemical reaction can be determined by the Gibbs free energy ( $\Delta G$ ) of the reaction which is dependent on the cell potential ( $E_{cell}$ ) by equation 7.7 below [23] with  $n$  transferred electrons, and  $F$  faraday's constant.

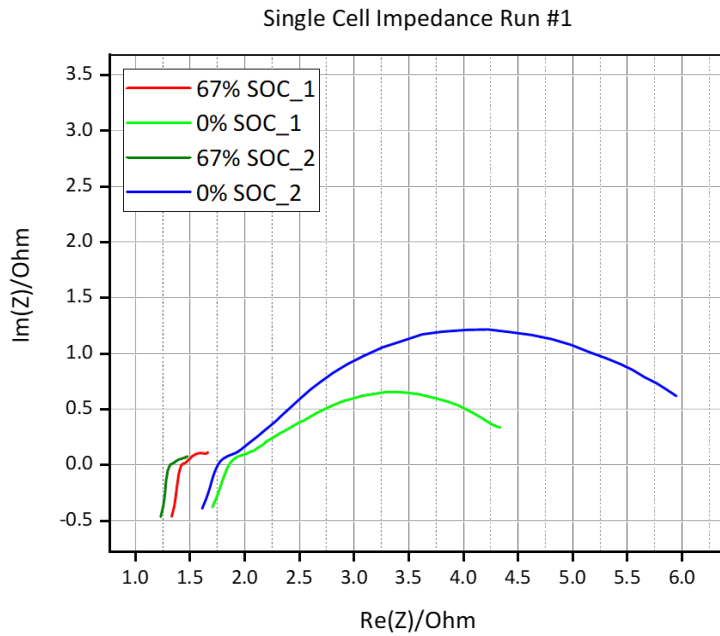


Figure 7.7: EIS Data of Single Cell with 2 charge cycles to 67% SoC

$$\Delta G [J] = -nE_{cell}F \quad (7.7)$$

This agrees with the open circuit cell potentials (OCP) determined for the full cell at 67 and 0% SoC, around 1.35 V and 0.7 V respectively. Calculating below, it is clear that the charged OCP produces a more negative Gibbs free energy, leading to a more spontaneous reaction.

$$\text{Charged: } \Delta G = -2 \cdot 1.35 \cdot 96485 \rightarrow -260.51 \text{ KJ} \quad (7.8)$$

$$\text{Discharged: } \Delta G = -2 \cdot 0.7 \cdot 96485 \rightarrow -135.01 \text{ KJ} \quad (7.9)$$

Analyzing the individual EIS feature differences between the charged and discharged curves of figure 7.7, it is evident that the free energy of the reactions leads to the decrease of the cell characteristic resistances. The semicircle feature corresponding to  $R_{ct}$  becomes very small when charged as the charge-transfer reaction at the anode occurs spontaneously. This decrease occurs as the oxidation of deposited Zn to Zn<sup>+2</sup> by equation 4.6 is thermodynamically favorable. In addition, the chemical gradient from a buildup of deposited Zn at the interface also leads to thermodynamic favorability of this reaction. The ohmic resistance of the cell  $R_{ohm}$ , the far left intersection of the impedance response with the real(Z) axis, is also seen

to decrease between charged and discharged. As this ohmic resistance is made up of contributions from the solution, contacts, and bulk materials in the cell, it is clear that this decrease is due to the change in the solution resistance portion. The contact and bulk material resistance do not change with SoC. Finally, the  $C_{dl}$  portion of the impedance response seen in the imaginary axis is shown to decrease as the concentration of charge-carriers at the anode/anolyte interface begin to decrease, weakening their double layer capacitive effect.

With cycling, the charge-transfer semi-circle can be seen to increase noticeably between the 1st and 2nd cycles at 0% SoC (light green and blue traces respectively). This could be due to the buildup of Zn deposits on the anode from incomplete discharging which leads to a greater resistance.

## Impedance Cells

After running EIS analysis on the full cell setup, it was important to understand how the impedance of each half cell was affected over the capacity range. To make successful EIS measurements of both half cells, two 'impedance cells' were added in series with the single cell at the outlets of both anode and cathode as shown in figure 6.5 above. These impedance cells did not include a separating membrane but only working and counter electrodes as described in section 6.1, so as to only be used as a tool to monitor each electrolyte half cell during the process.

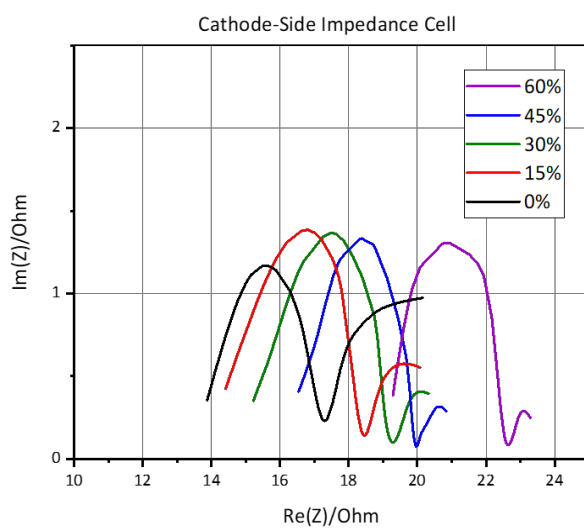


Figure 7.8: EIS Data of cathode-side impedance cell at charge states 0, 15, 30, 45, and 60% SoC

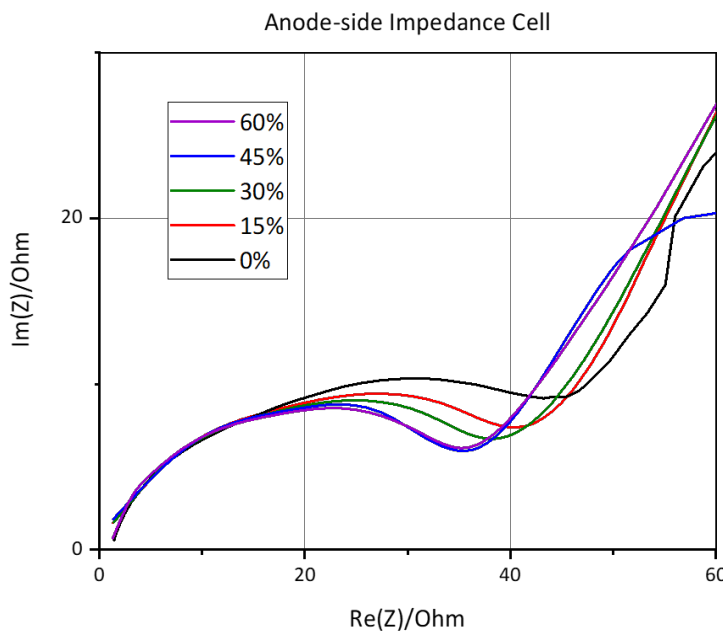


Figure 7.9: EIS Data of anode-side impedance cell at charge states 0, 15, 30, 45, and 60% SoC

Comparing the anode and cathode side impedance cell data above, it is immediately apparent that the half cells experience different electrochemical effects throughout the SoC of the full cell. With respect to the ohmic resistance, in the cathode impedance cell,  $R_{ohm}$  is seen to increase with SoC (fig. 7.8), while it remains constant for the anode impedance cell (fig. 7.9). The increase of  $R_{ohm}$  in the cathode cell is due to the increase in solution resistance as  $I^-$  is oxidized to  $I_3^-$ . As this oxidation occurs in the catholyte during charging, the number of free charge carriers decreases significantly as 3 moles of  $I^-$  ions are needed to produce 1 mole of  $I_3^-$  from equation 4.8. In addition,  $K^+$  ions migrate through the Nafion<sup>TM</sup> membrane from the catholyte to the anolyte to balance the charges between the two half cells. This decrease in the concentration of active charge carriers in the catholyte with charging leads to an increase in the solution resistance of the half cell and therefore  $R_{ohm}$ , shifting the impedance response to the right along the real(Z) axis.

On the anode-side half cell, a different shift in the impedance response is seen. Rather than the curves shifting along the x-axis, all of the curves maintain the same ohmic resistance throughout charge. Analyzing the ionic concentration changes of the anolyte, as the SoC increases, the concentration of  $Zn^{+2}$  decreases as it is reduced to a metallic thin film layer in the full cell on the thin carbon felt anode. Simultaneously, the concentration of  $K^+$  ions increases as they migrate through the membrane interlayer to balance the electrolyte charge due to this reduction.

Therefore, as the  $Zn^{+2}$  concentration decreases, the solution resistance stays constant due to this balance of  $K^+$  ions and the same shift along the  $Re(Z)$  axis is not seen as in 7.8. Instead the charge transfer semi-circle is seen to decrease in diameter with charge. As metallic Zn is deposited onto the anode, the surface area of the anode increases, creating more sites for charge transfer.

## Determination of Equivalent Circuit

An equivalent circuit was developed based on the known components and electrochemical processes occurring within the system. An ohmic resistance ( $R_{ohm}$ ) is first used to represent both the ionic resistance of the solution as well as the electronic resistance of the membrane and internal resistance of the electrodes. However, as these last two resistance components of the membrane and electrodes remains constant throughout cycling, this  $R_{ohm}$  component is used to monitor changes in solution resistance of the electrolytes.

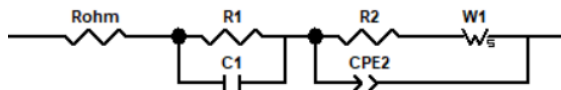


Figure 7.10: Equivalent circuit model of full cell

$R_1$  and  $R_2$  are used to represent the charge transfer resistances which occur at the electrode electrolyte interfaces at both anode and cathode. A double layer capacitance ( $C_1$ ) is in parallel with  $R_1$  to represent the capacitance formed at the inner and outer Helmholtz plane at the same electrode/electrolyte interface from a buildup of oppositely charged particles as they transfer their charge to the electrode. In order to represent a diffuse layer capacitance arising from a concentration gradient within the electrolyte, a constant phase element ( $CPE_2$ ) is used in parallel with  $R_2$ . Finally, a finite Warburg diffusion element ( $W_1$ ) is used to represent the diffusion processes occurring within the cell at low frequencies of the excitation perturbation of the EIS process. This diffusion characteristic is not present in the full cell impedance of figure 7.11.

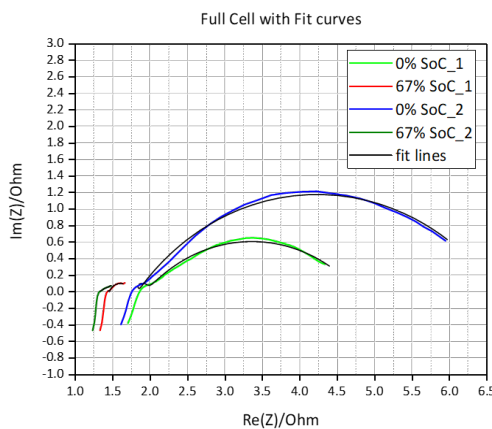


Figure 7.11: Impedance response data of figure 10.2 with fit curves.

Table 7.1: EIS fit data from the fit curves of figure 7.11 and the equivalent circuit of figure 7.10

Cycle	SoC	R <sub>ohm</sub> [Ω]	R1 [Ω]	C1 [F]	R2 [Ω]	CPE <sub>t</sub>	CPE <sub>p</sub>
1	0 %	1.79	0.16	5.84 E-5	2.83	0.09	0.52
	67%	1.44	0.02	4.01 E-10	0.30	1.25	0.75
2	0%	1.55	0.29	3.26E-06	4.80	0.06	0.58
	67%	1.31	0.02	4.90E-10	0.58	4.20	0.34

As seen from table of figure 7.1, the values of R<sub>ohm</sub> decrease after charge as well as between cycles as explained above. This is due to the changes in Gibbs free energy between charged and discharge state as well as the concentration gradient which both affect the favorability of the reaction and lower the solution resistance which is represented by R<sub>ohm</sub>. The t and p parameters of CPE (CPE<sub>t</sub> and CPE<sub>p</sub>) are related to the value of CPE in farads through the following expression.

$$CPE = \frac{1}{t(iw)^p} \quad (7.10)$$

### 7.3 Discussion and Further Improvements

With respect to further developments for this ZnI<sub>2</sub> flow chemistry, there are a few aspects of this system which could be adjusted to increase cell performance. Electrolyte conductivity and charge-transfer performance could be improved through adjustment of the electrolyte chemistry. The addition of another free charge carrier that would not be able to cross over the separating membrane may help to maintain a lower solution resistance. Since the Nafion<sup>TM</sup> membrane is a cation-exchange mem-

brane, meaning that only cations are able to pass through, perhaps this added free carrier species would need to be some kind of anion. Furthermore, with the addition of an anion charge carrier, the charge balance could be more easily maintained, decreasing the migration of  $K^+$  ions to the anolyte.

One way to help prevent the crossover of charge carriers could be to make modifications to the Nafion<sup>TM</sup> layer to make it less susceptible to anion movement. This could be carried out in multiple ways for example by coating the Nafion<sup>TM</sup> membrane with charged ions (either cations or anions) which would selectively reduce the cross-over of a certain species. The drawback of this approach would be an increase in the ohmic resistance of the membrane itself. Another way could be by modifying the Nafion<sup>TM</sup> polymer completely through polymer blending with another species such as polyvinylidene fluoride, which could lead to enhanced mechanical and electrochemical properties of the membrane. [43].

Another strategy which could help to decrease the solution resistance of the electrolyte is to all-together change the separating membrane to take advantage of different electrochemical properties. For example, an anion-exchange membrane could be used which would only allow transfer of anions. This membrane would prevent the transfer of  $K^+$  and  $Zn^{+2}$  ions meaning that only the concentration of  $Zn^{+2}$  ions on the anolyte side would contribute to the charge capacity of this half cell, possibly becoming a limiting factor for the overall cell capacity. Because of this, it may be necessary to increase the concentration of  $ZnI_2$  on the catholyte side if this option were to be implemented. Throughout the experimentation of these further developments, EIS can be employed as a valuable tool to monitor the changes in cell response that occur due to each of these adjustments.

# Chapter 8

## Environmental Impact Analysis

Throughout the course of this project, there were no direct emissions generated as the author used a bicycle for transportation to and from the place of work each day. However, there were indirect emissions generated from the laboratory and office work. For the calculation of indirect emissions seen in table 8.1, the electricity consumption of the author's laptop, and laboratory devices such as the computers, pump, and potentiostat were calculated. The average power of a laptop is 180 Watts. While being used 7 hours a day for 130 days, this works out to 163.8 kWh total. As for the potentiostat, it has a power of 600 W and is used approximately 6 hours a day for 60 days, totalling 216 kWh. Other lab equipment such as the computers, tube furnace are estimated to have consumed about 150 kWh throughout the project. Therefore, the energy usage works out to a total of 529.8 kWh. Using a value of 392 g CO<sub>2</sub>/kWh of electricity according to the Spanish energy mix, this works out to a total indirect emmissions of 207.682 kg of CO<sub>2</sub> generated from this project [44].

Table 8.1: Emission generated throughout project

Item	Power[W]	Use[hrs/day]	Days used	Total consumption[kWh]
Laptop	180	7	130	163.8
Potentiostat	600	6	60	216
Other equipment	-	-	-	150
Total [kWh]				529.8
<b>Total [kg of CO<sub>2</sub>]</b>				<b>207.682</b>

Waste was calculated to be negligible for this project as all materials were either saved for further analysis by other researchers or reused. No printing of research articles was done by the author in an effort to reduce paper waste. To reduce food packaging, a home-made lunch was brought by the author on most days. Support for the Fridays for Future student environmental strike was shown by the author on limited Fridays during this project duration.

# Chapter 9

## Economic Analysis

Costs related to the completion of this project are detailed below in table 9.1 according to the general categories of labor and materials.

For the purpose of calculating labor costs, the work hours of the author have been valued as equivalent hours for a junior research engineer while the advisors will be counted as senior engineers. The charges per working hour are approximate.

Table 9.1: Labor costs of project

Employee Position	Price per hour [€ /hr]	Working hours [hr]	Total price [€]
Junior Researcher	20	600	12,000
Senior Researcher 1	30	50	1,500
Senior Researcher 2	30	100	3,000
<b>Total</b>			<b>16,500</b>

Costs of materials used in this project were then calculated in table 9.2. Each piece of machinery used in this project was included. For machinery which have a longer lifetime than the course of this project, the estimated lifetime of the machine was used to calculate its cost. The prices for electrolyte chemicals and electrode reactants have been obtained from the official Sigma Aldrich and Fuel Cell store websites [45] [46].

Table 9.2: Materials/Machinery costs of project

Item	Total Cost [€]	Hours used/Total life	Total price [€]
Electrodes	56.50	.2	11.3
Electrolyte	341.29	.2	68.26
Membrane	61.60	.1	6.16
Impedance cells	405.15	.1	40.52
Full cell	57.85	.1	5.79
Pump	1200	0.1	120
Potentiostat	12,000	0.02	240
Tube Oven	350	.025	8.75
<b>Total</b>			<b>500.78</b>

Total costs were then calculated based on the sum of labor and material costs below.

$$C_{total} = C_{labor} + C_{materials} \rightarrow 17,000.78 \text{ Euros} \quad (9.1)$$

# Chapter 10

## Conclusion

After completion of this study, and analyzing the performance of a ZnI<sub>2</sub> redox flow battery directly in a laboratory environment, it is clear that this technology has great potential as an energy storage source for the next generation electrical grid. It has many beneficial characteristics over the current energy storage leader, Li-ion, such as decoupled power and energy, higher cycle life, higher availability and lower cost of materials, lower environmental impact, and simpler thermal management. Zn-I<sub>2</sub> chemistry also has less toxicity and better electrochemical kinetics than Zn-Br<sub>2</sub> batteries.

Electrochemical impedance spectroscopy of this ZnI<sub>2</sub> chemistry was able to provide some important information on the battery characteristics at different states of charge. In the full cell, the impedance characteristics were seen to decrease after charging to 67% SOC, indicating the thermodynamic favorability of the discharge reaction and following the trends of the Gibbs free energy. While these effects were evident for the full cell, it was unclear how the impedance changed in each half cell. To better understand this, two impedance cells were used to measure the half cell responses. It was evident from this response that the catholyte experienced an increase in ohmic resistance from charging while the anolyte showed a decrease in charge transfer resistance and double layer capacitance as the SoC increased. As the cell charged, the number of free charge carriers decreased in the catholyte, increasing the solution resistance and producing the shift along the real(Z) axis in the positive direction. In the anolyte, the solution resistance was unaffected however the charge transfer resistance was seen to decrease as the deposited zinc increased the anode surface area, creating additional sites for deposition and therefore facilitating charge transfer. With this clearer view of the half cell impedance responses of the system, it is easier to understand the limiting factors for the cell performance such as the depletion of charge carriers in the catholyte upon charging. Future improvements

were then proposed based on maintaining this concentration of charge carriers in the catholyte half cell such as addition of another electrolyte species or material adjustments to the separating membrane in order to change its electrochemical properties.

# Bibliography

- [1] Dieter Lüthi et al. “High-resolution carbon dioxide concentration record 650,000–800,000 years before present”. In: *Nature* 453.7193 (2008), pp. 379–382. ISSN: 14764687. DOI: 10.1038/nature06949.
- [2] Wolfram Schlenker and Charles A. Taylor. “Market expectations about climate change”. In: *National Bureau of Economic Research Working Paper Series* (2019).
- [3] IPCC. “Global Warming of 1.5 ° C: Chpt. 4: Strengthening and implementing the global response”. In: *IPCC Official Report* 1.June (2018).
- [4] International Energy Agency. *CO<sub>2</sub> Emissions Statistics*. 2019. URL: <https://www.iea.org/statistics/co2emissions/>.
- [5] International Energy Agency. “2018 World Energy Outlook: Executive Summary”. In: *IEA Report* (2018). URL: [www.iea.org/t&c/](http://www.iea.org/t&c/).
- [6] A. Zahedi. “Maximizing solar PV energy penetration using energy storage technology”. In: *Renewable and Sustainable Energy Reviews* 15.1 (2011), pp. 866–870. ISSN: 13640321. DOI: 10.1016/j.rser.2010.09.011. URL: <http://dx.doi.org/10.1016/j.rser.2010.09.011>.
- [7] IRENA. *Electricity Storage and Renewables: Costs and Markets To 2030*. October. IRENA, 2017. ISBN: 9789292600389. URL: [https://www.irena.org/-/media/Files/IRENA/Agency/Publication/2017/Oct/IRENA\\_Electricity\\_Storage\\_Costs\\_2017.pdf](https://www.irena.org/-/media/Files/IRENA/Agency/Publication/2017/Oct/IRENA_Electricity_Storage_Costs_2017.pdf).
- [8] International Renewable Energy Agency (IRENA). *Renewable Power Generation Costs in 2018*. 2018, p. 160. ISBN: 978-92-9260-040-2. DOI: 10.1007/SpringerReference\\_\\_7300. URL: [https://www.irena.org/-/media/Files/IRENA/Agency/Publication/2018/Jan/IRENA\\_2017\\_Power\\_Costs\\_2018.pdf](https://www.irena.org/-/media/Files/IRENA/Agency/Publication/2018/Jan/IRENA_2017_Power_Costs_2018.pdf).
- [9] Mauricio B.C. Salles et al. “Potential arbitrage revenue of energy storage systems in PJM”. In: *Energies* 10.8 (2017). ISSN: 19961073. DOI: 10.3390/en10081100.

- [10] L. Ren et al. “Techno-economic evaluation of hybrid energy storage technologies for a solar-wind generation system”. In: *Physica C: Superconductivity and its Applications* 484.1037 (2013), pp. 272–275. ISSN: 09214534. DOI: 10.1016/j.physc.2012.02.048. URL: <http://dx.doi.org/10.1016/j.physc.2012.02.048>.
- [11] U.S. Energy Information Administration. “Annual Energy Outlook 2017 with projections to 2050”. In: *EIA Annual Energy Outlook 2017* 44.8 (2017), pp. 1–64. ISSN: 1387-1811. DOI: DOE/EIA-0383(2017). URL: [https://www.eia.gov/outlooks/aeo/pdf/0383\(2017\).pdf](https://www.eia.gov/outlooks/aeo/pdf/0383(2017).pdf).
- [12] Abbas A Akhil et al. “DOE / EPRI 2013 Electricity Storage Handbook in Collaboration with NRECA Using Business Models for Storage Systems”. In: *Sandia Report* 1.July (2013). URL: <http://www.sandia.gov/ess/publications/SAND2013-5131.pdf>.
- [13] Piergiorgio Alotto, Massimo Guarneri, and Federico Moro. “Redox flow batteries for the storage of renewable energy: A review”. In: *Elsevier-Renewable and Sustainable Energy Reviews* 29 (2014), pp. 325–335. DOI: 10.1016/j.rser.2013.08.001.
- [14] Xing Luo et al. “Overview of current development in electrical energy storage technologies and the application potential in power system operation”. In: *Applied Energy* 137 (2015), pp. 511–536. ISSN: 03062619. DOI: 10.1016/j.apenergy.2014.09.081. URL: <http://dx.doi.org/10.1016/j.apenergy.2014.09.081>.
- [15] Fritz Crotogino, Klaus-Uwe Mohmeyer, and Roland Scharf. “Huntorf CAES: More than 20 Years of Successful Operation”. In: *Spring 2001 Meeting* 1.April (2001), pp. 1–7. URL: [http://www.uni-saarland.de/fak7/fze/AKE\\_Archiv/AKE2003H/AKE2003H\\_Vortraege/AKE2003H03c\\_Crotogino\\_ea\\_HuntorfCAES\\_CompressedAirEnergyStorage.pdf](http://www.uni-saarland.de/fak7/fze/AKE_Archiv/AKE2003H/AKE2003H_Vortraege/AKE2003H03c_Crotogino_ea_HuntorfCAES_CompressedAirEnergyStorage.pdf).
- [16] Francisco Diaz-Gonzalez. “Module 2 . Overview of energy storage technologies”. In: *UPC lecture* (2018).
- [17] Eduard Oró et al. “Comparative life cycle assessment of thermal energy storage systems for solar power plants”. In: *Renewable Energy* 44 (2012), pp. 166–173. ISSN: 09601481. DOI: 10.1016/j.renene.2012.01.008. URL: <http://dx.doi.org/10.1016/j.renene.2012.01.008>.

- [18] Rainer Tamme et al. *Thermal Energy Storage*. May. Elsevier Inc., 2013, pp. 688–714. ISBN: 9780124095489. DOI: 10.1007/978-1-4614-5806-7\\_\\_684. URL: <http://dx.doi.org/10.1016/B978-0-12-409548-9.01064-2>.
- [19] United States Department of Energy. *2014: The Year of Concentrating Solar Power*. 2014.
- [20] Nishant Kumar. “Superconducting Magnetic Energy Storage ( SMES ) Program”. In: *Research Gate* 1.July (2015).
- [21] Fior Markets. *Global Superconducting Magnetic Energy Storage (SMES) Systems Market Research Report 2018-2025*. Tech. rep. 2019.
- [22] Dra.Teresa Andreu. *Lesson 5- Advanced Materials for Enabling Energy Transformation*. 2016.
- [23] M. Skyllas-Kazacos, C. Menictas, and T. Lim. *Redox flow batteries for medium-to large-scale energy storage*. Woodhead Publishing Limited, 2013, pp. 398–441. ISBN: 9781845697846. DOI: 10.1533/9780857097378.3.398. URL: <http://dx.doi.org/10.1533/9780857097378.3.398>.
- [24] Wanqiu Liu et al. “Aqueous Flow Batteries: Research and Development”. In: *ChemPubSoc Europe* (2018), pp. 1–17. DOI: 10.1002/chem.201802798.
- [25] Bo Hu et al. “Redox-Active Inorganic Materials for Redox Flow Batteries”. In: *Encyclopedia of Inorganic and Bioinorganic Chemistry* (2019), pp. 1–25. DOI: 10.1002/9781119951438.eibc2679.
- [26] M. C. Wu et al. “Carbonized tubular polypyrrole with a high activity for the Br<sub>2</sub>/Br redox reaction in zinc-bromine flow batteries”. In: *Electrochimica Acta* 284 (2018), pp. 569–576. ISSN: 00134686. DOI: 10.1016/j.electacta.2018.07.192.
- [27] Jae Deok Jeon et al. “Dual function of quaternary ammonium in Zn/Br redox flow battery: Capturing the bromine and lowering the charge transfer resistance”. In: *Electrochimica Acta* 127 (2014), pp. 397–402. ISSN: 00134686. DOI: 10.1016/j.electacta.2014.02.073. URL: <http://dx.doi.org/10.1016/j.electacta.2014.02.073>.
- [28] Bin Li et al. “Ambipolar zinc-polyiodide electrolyte for a high-energy density aqueous redox flow battery”. In: *Nature Communications* 6 (2015), pp. 1–8. DOI: 10.1038/ncomms7303. URL: <http://dx.doi.org/10.1038/ncomms7303>.
- [29] Congxin Xie et al. “A Long Cycle Life , Self-Healing Zinc – Iodine Flow Battery with High Power Density”. In: *Angewandte Chemie* 100039 (2018), pp. 11171–11176. DOI: 10.1002/anie.201803122.

- [30] Guo-ming Weng et al. “Unlocking the capacity of iodide for high-energydensity zinc/polyiodide and lithium/polyiodide redox flow batteries”. In: *Energy & Environmental Science* 10 (2017), pp. 735–741. DOI: 10.1039/C6EE03554J. URL: <http://dx.doi.org/10.1039/C6EE03554J>.
- [31] Jing Zhang et al. “An all-aqueous redox flow battery with unprecedeted energy density”. In: *Energy and Environmental Science* 11.8 (2018), pp. 2010–2015. ISSN: 17545706. DOI: 10.1039/c8ee00686e.
- [32] Congxin Xie et al. “Environmental Science with super high energy density for stationary energy storage”. In: *The Royal Society of Chemistry* (2019). DOI: 10.1039/C8EE02825G.
- [33] Jun Lu, Tianpin Wu, and Khalil Amine. “State-of-the-art characterization techniques for advanced lithium-ion batteries”. In: *Nature Energy* 2.3 (2017). ISSN: 20587546. DOI: 10.1038/nenergy.2017.11.
- [34] Z. Tang. “Characterization Techniques and Electrolyte Separator Performance Investigation for All Vanadium Redox Flow Battery”. In: (2013), p. 205. URL: [http://trace.tennessee.edu/utk\\_graddiss/2620/](http://trace.tennessee.edu/utk_graddiss/2620/) %5Cn[http://trace.tennessee.edu/cgi/viewcontent.cgi?article=3614&context=utk\\_graddiss](http://trace.tennessee.edu/cgi/viewcontent.cgi?article=3614&context=utk_graddiss).
- [35] Vadim F. Lvovich and A John Wiley. *Impedance Spectroscopy: Applications to Electrochemical and Dielectric Phenomena*. John Wiley & Sons, Inc., 2012, p. 353. ISBN: 9780470627785.
- [36] Y. Ashraf Gandomi et al. “Critical Review—Experimental Diagnostics and Material Characterization Techniques Used on Redox Flow Batteries”. In: *Journal of The Electrochemical Society* 165.5 (2018), A970–A1010. ISSN: 0013-4651. DOI: 10.1149/2.0601805jes.
- [37] Alan M Pezeshki et al. “Elucidating effects of cell architecture , electrode material , and solution composition on overpotentials in redox flow batteries”. In: *Electrochimica Acta journa* 229 (2017), pp. 261–270.
- [38] Chong Bai et al. “A sustainable aqueous Zn-I<sub>2</sub> battery”. In: *Nano Research* 11.7 (2018).
- [39] Huilin Pan et al. “Controlling Solid Liquid Conversion Reactions for a Highly Reversible Aqueous Zinc Iodine Battery”. In: *ACS Energy Letters* (2017), pp. 6–12. DOI: 10.1021/acsenergylett.7b00851.
- [40] Elsevier Scopus Database. *Scopus Search, ( ALL ( 'zinc-iodide' OR 'zn-i2' OR 'zni2' ) ) AND ( impedance )*. 2019.

- [41] Chakraborty M et al. “Design optimization of low cost, highly efficient aqueous zinc-iodide flow battery”. In: *Poster Contribution* (2019).
- [42] Ruiyong Chen et al. “Redox Flow Batteries: Fundamentals and Applications”. In: *InTech* (2017). DOI: 10.5772/intechopen.68752.
- [43] Helen Prifti et al. “Membranes for Redox Flow Battery Applications”. In: *Membranes* (2012), pp. 275–306. DOI: 10.3390/membranes2020275.
- [44] Generalitat de Catalunya. *Emissions per kWh segons el mix energètic espanyol de 2017*. Tech. rep. 2017. URL: [http://canviclimatic.gencat.cat/es/reduceix\\_emissions/com-calcular-emissions-de-geh/factors\\_demissio\\_associats\\_a\\_lenergia/](http://canviclimatic.gencat.cat/es/reduceix_emissions/com-calcular-emissions-de-geh/factors_demissio_associats_a_lenergia/).
- [45] Sigma Aldrich. *Sigma Aldrich online store*. 2019. URL: <https://www.sigmaaldrich.com/spain.html>.
- [46] Fuel cell store Online. *Fuel Cell online store*. 2019. URL: <https://www.fuelcellstore.com/>.

# Appendix

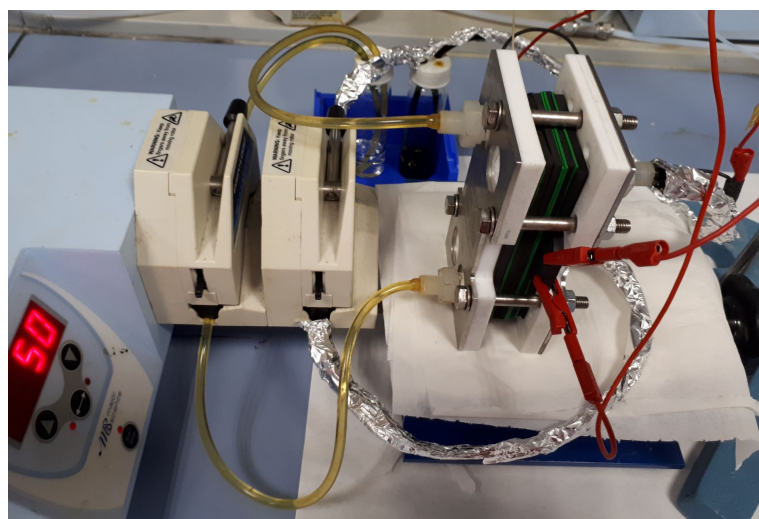


Figure 10.1: Single cell setup from first EIS runs [41]

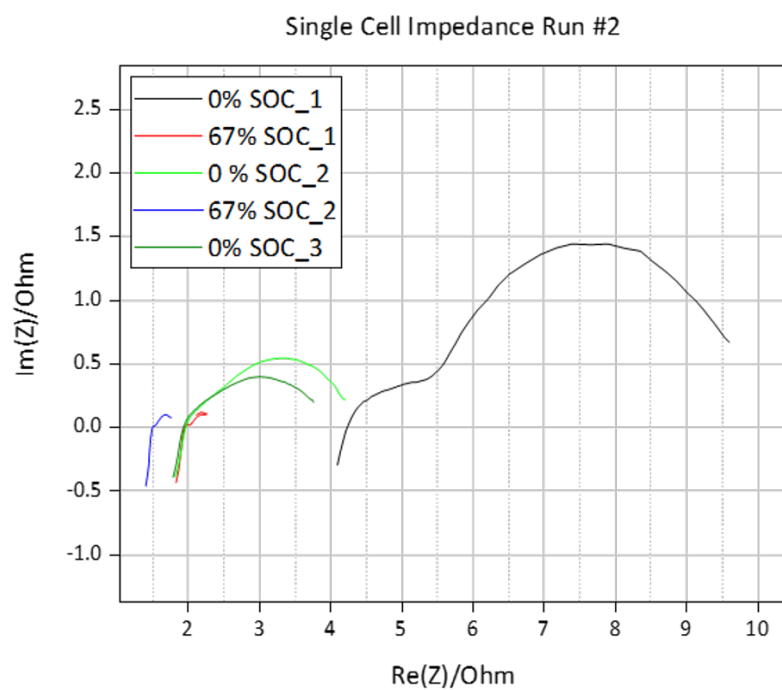


Figure 10.2: EIS run #2 of single cell setup

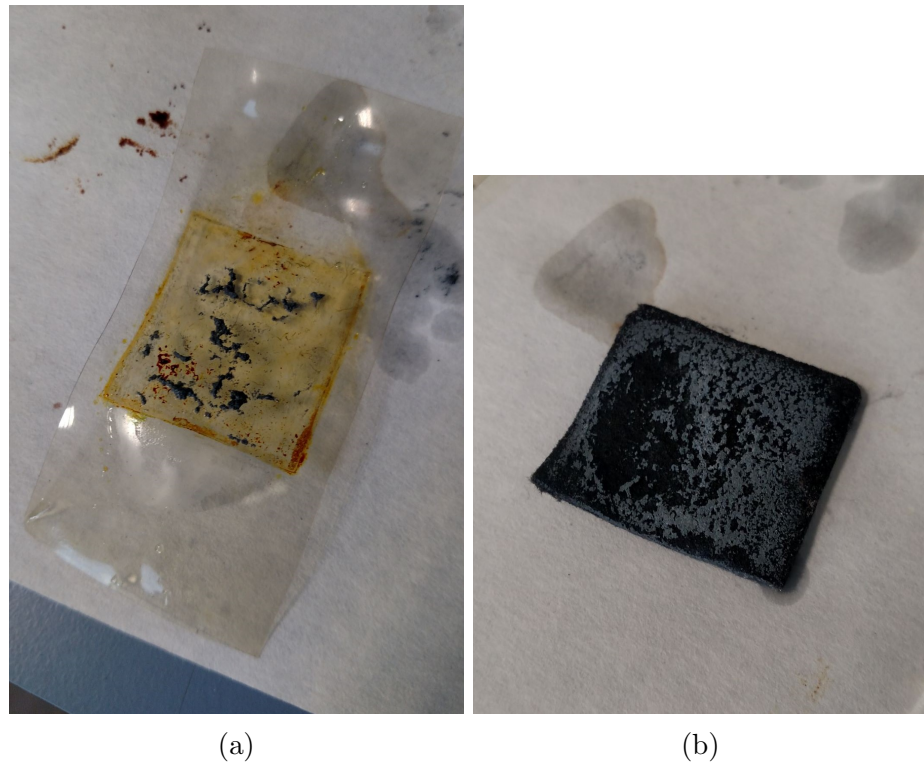


Figure 10.3: Nafion membrane (a), and carbon felt (b) anode after cycling